Published in final edited form as:
Astrophys J. 2015 October 10; 812(1): . doi:10.1088/0004-637X/812/1/75.

VELOCITY-RESOLVED [C II] EMISSION AND [C II]/FIR MAPPING ALONG ORION WITH *HERSCHEL* *,**

Javier R. Goicoechea[1], **D. Teyssier**[2], **M. Etxaluze**[1,3], **P.F. Goldsmith**[4], **V. Ossenkopf**[5], **M. Gerin**[6,7], **E.A. Bergin**[8], **J.H. Black**[9], **J. Cernicharo**[1], **S. Cuadrado**[1], **P. Encrenaz**[6], **E. Falgarone**[6,7], **A. Fuente**[10], **A. Hacar**[11], **D.C. Lis**[6], **N. Marcelino**[12], **G.J. Melnick**[13], **H.S.P. Müller**[5], **C. Persson**[9], **J. Pety**[14], **M. Röllig**[5], **P. Schilke**[5], **R. Simon**[5], **R.L. Snell**[15], and **J. Stutzki**[5]

[1]Instituto de Ciencia de Materiales de Madrid (CSIC). Calle Sor Juana Ines de la Cruz 3, E-28049 Cantoblanco, Madrid, Spain

---

**Herschel* is an ESA space observatory with science instruments provided by European-led Principal Investigator consortia and with important participation from NASA.

**Uses observations obtained with the IRAM-30m telescope. IRAM is supported by INSU/CNRS (France), MPG (Germany), and IGN (Spain).

[3]In this work we refer to the *luminosity* (L) computed in power units (erg s^{-1} or $L_\odot$). The conversion from velocity-integrated line intensities $\int \Delta T_b \, d_v = W$ (K km s^{-1}), with ΔT_b the continuum-subtracted brightness temperature (see Section 2), to line surface brightness (I), is I=2k W ν^3/c^3. For the [C II] 158 μm and CO J=2-1 lines respectively, the conversion is I (erg s^{-1} cm^{-2} sr^{-1})=7.0×10^{-6} W (K km s^{-1}) and 1.3×10^{-8} W (K km s^{-1}).

[4]HIPE is a joint development by the Herschel Science Ground Segment Consortium, consisting of ESA, the NASA Herschel Science Center, and the HIFI, PACS, and SPIRE consortia.

[5]See: http://herschel.esac.esa.int/twiki/pub/Public/HifiCalibrationWeb/HifiBeamReleaseNote_Sep2014.pdf

[6]L_{FIR} from 40 to 500 μm (Sanders & Mirabel 1996) and using D=414 pc.

[7]The central region of the photometric image (BN/KL outflows and IRc sources) contain saturated data points that are not used in our analysis.

[8]The Orion A molecular complex to which OMC 1 belongs shows a velocity gradient of 0.7 km s^{-1} pc^{-1} over ~25 pc (e.g., Bally et al. 1987).

[9]Line luminosity per pixel integrating all [C II] spectral components.

[10]Using N_H (cm^{-2}/pixel) = N(H) + 2 N(H$_2$) = $M_{Gas}/(\mu \, m_H \, D^2 \, \Omega)$, with M_{Gas} obtained from Equation (2).

[11]At the distance of OMC 1 and considering the pixel size in Fig. 8(a), the L_{FIR} scale per pixel is equivalent to $G_0 \approx 200 \, L_{FIR}/L_\odot$ (per pixel). This relation neglects dust heating by embedded sources. Here we assume that owing to the high FUV field in the region, this extra heating does not dominate at large scales. For the same reason, and owing to the warm dust grain temperatures, we neglect the dust emission at >500 μm in the G_0 estimation.

[12]Corrected line strengths for the [^{13}C II] F=2-1, 1-0 and 1-1 hyperfine lines at 1900.466, 1900.950 and 1900.136 GHz respectively have been published by Ossenkopf et al. (2013). The relative line strengths are 0.625, 0.250 and 0.125. These are slightly different from those of Cooksy et al. (1986) that were used in the analysis of Stacey et al. (1991b) and Boreiko & Betz (1996), and resulted in ^{12}C/^{13}C isotopic ratios lower than the usual value of 67.

[13]Toward the Orion Bar and BN/KL, the [^{13}C II] F=2-1 line is blended with the red-shifted [C II] emission. To avoid overestimating the [C II] 158 μm line opacity toward these positions, we used the [^{13}C II] F=1-0 line (which is not blended with any spectral feature) and assumed I[^{13}C II] = $I_{F=1-0}$/0.250.

[14]Scaling our data by L_{FIR}(40-500 μm)≃1.5 $L_{42-122\mu m}$ and assuming $I_{CO\ 2-1} \simeq 8 I \, I_{CO\ 1-0}$ (erg s^{-} cm^{-2} sr^{-}) for optically thick thermalized CO gas.

[15]In the most general case, $I_{[CII]}/I_{FIR} \simeq I_{[CII]}(T_k)/[\int B_\lambda(T_d)(1-e^{-\tau_{d,\lambda}})d\lambda]$, with T_k and T_d only coupled inside clouds at high densities n>10^6 cm^{-3}. For the 1σ range of T_d and $\tau_{d,160}$ values toward OMC 1, I[C II]/I_{FIR} can be approximated by $I_{[CII]}/I_{FIR} \approx C \cdot I$[C II]/[$B_{160}(T_d)(1-e^{-\tau_{d,160}})$], with the C constant varying a factor of ~2 depending on the exact T_d and $\tau_{d,160}$ values. Thus, if T_d does not vary much, the FIR intensity raises with increasing total column density through the cloud, as shown in Figure 11(b).

[16]At the average distance of ~4 kpc of these massive star-forming regions, the ~50″×50″ mapped areas are equivalent to ~1×1 pc^2. The typical spatial resolution toward these more distant SFR regions with *Herschel* is ~0.2 pc.

[2]Herschel Science Centre, ESA/ESAC, P.O. Box 78, Villanueva de la Cañada, E-28691 Madrid, Spain

[3]RAL Space, Rutherford Appleton Laboratory, Didcot OX11 0QX, UK

[4]Jet Propulsion Laboratory, California Institute of Technology, 4800 Oak Grove Drive, Pasadena, CA 91109-8099, USA

[5]I. Physikalisches Institut der Universität zu Köln, Zülpicher Str. 77, 50937 Köln, Germany

[6]LERMA, Observatoire de Paris, PSL Research University, CNRS, Sorbonne Universités, UPMC Univ. Paris 06, F-75014, Paris, France

[7]École Normale Supérieure, 24 rue Lhomond, F-75005, Paris, France

[8]Department of Astronomy, University of Michigan, 500 Church Street, Ann Arbor, MI 48109, USA

[9]Department of Earth and Space Sciences, Chalmers University of Technology, Onsala Space Observatory, SE-43992 Onsala, Sweden

[10]Observatorio Astronómico Nacional (OAN IGN), Apdo. 112, 28803, Alcalá de Henares, Spain

[11]Institute for Astrophysics, University of Vienna, Türkenschanzstrasse 17, 1180, Vienna, Austria

[12]INAF, Istituto di Radioastronomia, via P. Gobetti 101, 40129, Bologna, Italy

[13]Harvard-Smithsonian Center for Astrophysics, 60 Garden Street, MS 66, Cambridge, MA 02138, USA

[14]Institut de Radioastronomie Millimétrique, 300 rue de la Piscine, 38406 Saint-Martin d'Héeres, France

[15]Department of Astronomy, University of Massachusetts, LGRT-B 619E, 710 North Pleasant Street, Amherst, MA 01003, USA

Abstract

We present the first ~$7.5' \times 11.5'$ velocity-resolved (~0.2 km s^{-1}) map of the [C II] 158 μm line toward the Orion molecular cloud 1 (OMC 1) taken with the *Herschel*/HIFI instrument. In combination with far-infrared (FIR) photometric images and velocity-resolved maps of the H41α hydrogen recombination and CO J=2-1 lines, this data set provides an unprecedented view of the intricate small-scale kinematics of the ionized/PDR/molecular gas interfaces and of the radiative feedback from massive stars. The main contribution to the [C II] luminosity (~85 %) is from the extended, FUV-illuminated face of the cloud (G_0>500, n_H>5×10^3 cm^{-3}) and from dense PDRs ($G \gtrsim 10^4$, $n_H \gtrsim 10^5$ cm^{-3}) at the interface between OMC 1 and the H II region surrounding the Trapezium cluster. Around ~15 % of the [C II] emission arises from a different gas component without CO counterpart. The [C II] excitation, PDR gas turbulence, line opacity (from [^{13}C II]) and role of the geometry of the illuminating stars with respect to the cloud are investigated. We construct maps of the L[C II]/L_{FIR} and L_{FIR}/M_{Gas} ratios and show that L[C II]/L_{FIR} decreases from the extended cloud component (~10^{-2}–10^{-3}) to the more opaque star-forming cores (~10^{-3}–10^{-4}). The lowest values are reminiscent of the "[C II] deficit" seen in local ultra-luminous IR galaxies hosting vigorous star formation. Spatial correlation analysis shows that the decreasing L[C II]/L_{FIR} ratio correlates better with the column density of dust through the molecular cloud than with

$L_{\rm FIR}/M_{\rm Gas}$. We conclude that the [C II] emitting column relative to the total dust column along each line of sight is responsible for the observed L[C II]/$L_{\rm FIR}$ variations through the cloud.

Keywords

H II regions; galaxies: ISM; infrared: galaxies; ISM: clouds

1. INTRODUCTION

The $^2P_{3/2}$-$^2P_{1/2}$ fine structure line ($\Delta E/k \simeq 91$ K) of ionized carbon, [C II] 158 μm, is one of the most important cooling lines of the cold neutral medium (Dalgarno & McCray 1972) and among the brightest lines in photodissociation regions (PDRs, e.g., Hollenbach & Tielens 1999). Early observations showed that the line is very luminous (Russell et al. 1980), carrying from ~0.1 to 1 % of the total far-IR (FIR) luminosity of galaxies (Crawford et al. 1985). The neutral carbon atom has an ionization potential of 11.3 eV, so that the ion C^+ traces the H^+/H/H_2 transition, the critical conversion from atomic to molecular ISM. As a consequence, [C II] emission/absorption from different ISM phases is expected. Recent velocity-resolved line surveys show that the average contribution to the [C II] emission in the Milky Way is the H_2 gas illuminated by far-UV (FUV; $E \simeq 6$-13.6 eV) photons (55-75 %), the cold atomic gas (20-25 %) and the H II ionized gas (5-20 %) (Pineda et al. 2013, 2014).

Star-forming complexes hosting massive OB stars are irradiated by strong FUV fields and most of their [C II] emission is likely to arise from dense PDRs at the interface between H II regions and their parental molecular cloud (e.g., Stacey et al. 1993). Therefore, the [C II] 158 μm line traces the FUV radiation field from massive stars and indirectly, the star formation rate (SFR) (e.g., Stacey et al. 2010; Pineda et al. 2014; Herrera-Camus et al. 2015). As in the Milky Way, the [C II] emission in nearby galaxies is widespread and ultimately related to the star formation activity (Rodriguez-Fernandez et al. 2006; Malhotra et al. 2001; Kapala et al. 2015). In addition, an undetermined fraction of the [C II] arises from the diffuse neutral gas (Madden et al. 1993) and from the H II ionized gas, the latter varying from ≈5 to 50%, depending on the ionizing radiation strength and electron density (e.g., Abel 2006a).

In normal and starburst galaxies, the [C II]-to-FIR luminosity[3] ratio (L[C II]/L_{FIR}) is in the 10^{-2} to 10^{-3} range. Low metallicity dwarf galaxies show the highest ratios ($\gtrsim 10^{-2}$, e.g., Madden et al. 1997), whereas observations with *ISO* showed that local ultra-luminous galaxies (ULIRGs, $L_{\rm FIR} > 10^{12}\ L_\odot$) display a deficiency, L[C II]/$L_{FIR} \simeq 10^{-4}$, that is not straightforward to interpret (Malhotra et al. 1997; Luhman et al. 1998). This fractional luminosity deficiency has been confirmed with new observations of ULIRGs, hosting intense star formation and often associated with galaxy mergers (e.g., Graciá-Carpio et al. 2011; González-Alfonso et al. 2015). This deficit, however, does not necessarily hold in the early Universe at high-z (e.g., Stacey et al. 2010; Brisbin et al. 2015).

Interestingly, while it is difficult from the ground to detect the [C II] emission in the local Universe (balloon, airborne, or space telescopes are needed to overcome the low atmospheric transmission at 158 μm), the line does become accessible to ground-based

Europe PMC Funders Author Manuscripts

submm observatories such as ALMA at redshifts z >1. Indeed, the [C II] line has been detected toward young z > 5 galaxies (Riechers et al. 2014; Capak et al. 2015).

Most of the [C II] emission arising from PDR gas in the Milky Way is associated with modest average FUV radiation fields, between $G_0 \simeq 1$-20 (Pineda et al. 2013) and $G_0 \simeq 100$ (Cubick et al. 2008), with G_0 the mean interstellar FUV field in Habing units (G_0=1 is equal to 1.6×10^{-3} erg cm^{-2} s^{-1}, Habing 1968). These radiation fields are likely not representative of the efficient massive star forming modes expected in ULIRGs showing L[C II]/L_{FIR} deficits. Galactic high-mass star-forming regions, however, offer a more interesting template in which to investigate the [C II] emission in the more extreme irradiation conditions prevailing these active galaxies. The Orion molecular cloud 1 (OMC 1), in the Orion A complex, lies behind the Orion Nebula cluster (e.g., O'Dell 2001) and is the nearest (~414 pc), and probably most studied high-mass star-forming region of the Milky Way (e.g., Genzel & Stutzki 1989).

OMC 1 is directly exposed to the UV radiation emitted by young massive stars in the Trapezium cluster, located ~0.3 pc in front of the molecular cloud (e.g., Bally 2008). A region of several parsecs in size is exposed to FUV fluxes much higher than the average G_0 in the Milky Way (e.g., Stacey et al. 1993; Luhman et al. 1994; Rodriguez-Franco et al. 1998). The Trapezium stars have created a blister H II region that on the far side is bounded by the molecular cloud. The most famous H II/OMC 1 interface is the Orion Bar PDR (the "Bright Bar" seen in the visible-light images), a protrusion of OMC 1 in which the neutral cloud acquires a nearly edge-on geometry and thus the optically thin PDR emission is limb-brightened (Hogerheijde et al. 1995; Cuadrado et al. 2015, and references therein). On the near side, toward the observer, several components of neutral atomic gas revealed by H I absorption cover the nebula, the Orion's Veil (e.g., van der Werf et al. 2013).

Intermediate- and high-mass star formation is currently taking place in two locations: the Becklin-Neugebauer/Kleinmann-Low (BN/KL) region within OMC 1 (Blake et al. 1987; Tercero et al. 2010), and Orion South (S), an isolated molecular core located within the ionized gas cavity in front of OMC 1 (e.g., O'Dell et al. 2009). Therefore, Orion is a unique region to study the spatial distribution of [C II] and related quantities (L[C II]/L_{FIR}, L[C II]/$L_{\rm CO}$, $L_{\rm FIR}$/$M_{\rm Gas}$, etc.) in well characterized environments (dense PDRs, shocks, H II regions, and lower density quiescent gas).

The [C II] 158 μm line has been previously mapped toward OMC 1 at low angular (~55″) and spectral (~67 km s^{-1}) resolution with the *Kuiper Airborne Observatory* (KAO, Stacey et al. 1993; Herrmann et al. 1997) and also with balloon-borne FIR telescopes (e.g., Mookerjea et al. 2003). Pointed observations toward the Trapezium cluster region were also carried out by Boreiko & Betz (1996) with a heterodyne receiver on board KAO. These observations employed a velocity resolution of 0.5 km s^{-1} and allowed the detection of two of the three [^{13}C II] hyperfine line components. The HIFI instrument (de Graauw et al. 2010) on board *Herschel* (Pilbratt et al. 2010) allowed us to spectrally resolve (~0.2 km s^{-1} resolution) and to map the [C II] 158 μm line with unprecedented sensitivity and angular resolution (~11.4″). Velocity-resolved spectroscopy offers the best way to characterise the origin of all possible [C II] emission components and their kinematics. In addition, it allows one to map [^{13}C II]

Europe PMC Funders Author Manuscripts

and estimate the [C II] line opacity, a critical parameter to determine C^+ column densities (Stacey et al. 1991b; Boreiko & Betz 1996; Goldsmith et al. 2012; Ossenkopf et al. 2013).

In this work, we present initial results from a *Herschel* Open-Time program (OT1_jgoicoec_4) devoted to the spatial and velocity structure of the ionized and the warm molecular gas in OMC 1. In particular we present a large-scale velocity-resolved map of the [C II] 158 μm line, complemented by a map of the H41α recombination line, and existing CO J=2-1 and FIR photometric observations. The paper is organized as follows. In Section 2 we present the data set. The [C II] spatial distribution and gas kinematics is studied in Section 3. In Section 4 we analyze the [C II] 158 μm non-LTE excitation and derive C^+ column densities. A spatial correlation analysis of different quantities often used in the extragalactic discussion is also carried out. Finally, our results are discussed in the context of the [C II], CO and FIR diagnostic power and their link with the extragalactic emission.

2. OBSERVATIONS AND DATA REDUCTION

2.1. [C II], *H41α and CO 2-1 Heterodyne Observations*

The [C II] line at 1900.537 GHz (Cooksy et al. 1986) was mapped over a total area of ~7.5′×11.5′ (~0.9 pc ×1.4 pc) in 2012 August, using the HIFI instrument on board *Herschel*. A pair of Hot Electron Bolometer mixers was employed to observe the [C II] line in HIFI band 7b in two orthogonal polarizations. We used the Wide Band Acousto-Optical Spectrometer providing a spectral resolution of 1.1 MHz and a bandwidth of 2.4 GHz ($\simeq$0.2 km s^{-1} and $\simeq$380 km s^{-1} at 1900.5 GHz, respectively).

Three ~7.5′×4′ On-The-Fly (OTF) submaps of 3 h each were needed to cover the region with a 10″ sampling (ObsIDs: 1342250415, 1342250414 and 1342250412). The half-power beam width (HPBW) of HIFI at these frequencies is ~11.4″, i.e., the map is not fully sampled. Because of the large scale [C II] emission (Stacey et al. 1993) and risk of contaminating emission in the reference position, the OTF maps were performed using the Load-Chop referencing scheme (Roelfsema et al. 2012). In this mode, an internal chopper alternates between the sky and an internal cold load as the telescope slews over a scan leg. Although a nearby reference position (at a radial offset of ~ 9′ from the map centre) was also observed, we reprocessed the data without subtracting this reference emission from the on-source data, therefore being insensitive to line contamination from self-chopping. The resulting data are mostly affected by so-called Electrical Standing Waves, that were removed in HIPE[4] using the *doHebCorrection* task (Kester et al. 2014). The residual optical standing waves resulting from resonances against the internal hot load (~100 MHz period) and the diplexer optics (~625 MHz) were treated using the *FitHifiFringe* task in HIPE. The three sub-maps were then compared pair by pair in a region of ~7.5′×0.6′ where they overlap on the sky. Antenna temperatures (T_A^*) were extracted for each overlapping pixel and [C II] velocity channel. Scatter plots were formed to derive the inter-calibration factor between the respective coverage in each channel. We derived linear slopes deviating from unity by ~5% between pairs of sub-maps. Since we cannot know a priori which map corresponds to the true intensity, we re-adjusted the fluxes by ±2.5% depending on the sub-map, i.e. re-calibrated with respect to the mean intensities in the overlapping regions.

Through this work we use the main beam temperature scale (T_{mb} in K) as opposed to T^*_A. Given the latest HIFI efficiencies, both scales[5] are related by $T_{mb} \simeq 1.64\, T^*_A$. For semi-extended (not infinite but larger than the main beam width of *Herschel*/HIFI) emission sources of uniform brightness temperature (T_b), the main beam temperature is the most appropriate intensity scale ($T_{mb} \simeq T_b$). The achieved rms noise was typically ~1.5 K (1σ) per 0.2 km s^{-1} resolution channel and position. This rms is only a factor of ~2.5 worse than that achieved by Boreiko & Betz (1996) in their deep pointed observations after an integration of ~3 h. Figure 1 (right) shows the baseline-subtracted [C II] integrated line intensity map.

The H41α millimeter recombination line at 92.034 GHz was mapped with the IRAM-30m telescope at Pico Veleta (Spain) using the E090 receiver and the 200 kHz FFTS backend in 2013 November. The HPBW at this frequency is ~27″ and the typical rms noise in the map is low, ~0.05 K per 0.65 km s^{-1} resolution channel. In this work we also make use of part of the high-sensitivity CO 2-1 large-scale map (1×0.8°) at 230.538 GHz obtained by Berné et al. (2014) with the multi-beam receiver HERA, also at the IRAM-30m telescope. The spectral and angular resolutions are 320 kHz and ~11″, respectively. The achieved rms noise is ≃0.2 K per 0.4 km s^{-1} channel (see Berné et al. 2014). Both H41α and CO 2-1 OTF maps are fully sampled.

Herschel/HIFI and IRAM-30m data were processed with the GILDAS/CLASS software. Figures 1, 6, and 7 show the [C II] 158 μm, H41α and CO 2-1 emission at their native angular resolutions but resampled to a common velocity grid of 0.65 km s^{-1}. Offsets of selected positions are given with respect to the center of the [C II] map: α_{2000}: $5^h35^m17.0^s$, δ_{2000}: −5°22′33.7″. Table 1 summarizes the main spectroscopic parameters of the lines discussed in this work. To match the FIR photometric observations and carry out a combined analysis, the line maps were also gridded and convolved to an uniform angular resolution of 25″ (~0.05 pc).

2.2. *Photometric Observations and SED Fits*

In order to determine the FIR luminosity[6] and the dust continuum opacity toward each position of the [C II] map, we also make use of fully sampled calibrated images of OMC 1 taken with the *Herschel*/SPIRE and PACS[7] cameras (Griffin et al. 2010; Poglitsch et al. 2010) at 70, 160, 250, 350 μm photometric bands (from programs GT2_pandre and OT1_nbillot), and with JCMT/SCUBA2 at 850 μm (project JCMTCAL; Holland et al. 2013).

We convolved all the photometric images to a 25″ resolution (that of the 350 μm image) and fitted the resulting spectral energy distribution (SED) per 12.5″-pixel with a modified black body at an *effective* dust temperature (T_d);

$$F_\lambda = B_\lambda(T_d) \cdot \left(1 - e^{-\tau_{d,\lambda}}\right) \cdot \Omega \quad (1)$$

where Ω is the solid angle subtended by each pixel. Fit examples are shown in the Appendix. The dust continuum opacity is parametrized as $\tau_{d,\lambda} = \tau_{d,160}(160/\lambda)^\beta$, with $\tau_{d,160}$ the dust opacity close to the [C II] 158 μm line, and β a grain emissivity index. The resulting L_{FIR} and $\tau_{d,160}$ maps, where we have allowed β to be a free parameter of the fits, are shown in Figures

Europe PMC Funders Author Manuscripts

8(a) and (f). The mean β value is 2.4±0.5 (1σ) but we note that the derived FIR luminosities and dust opacities, the relevant quantities for our analysis, do not change significantly by fixing β to a constant value of 2. We also estimated the pixel-averaged gas column density and mass. In particular, we used the SPIRE 250 μm image assuming that it corresponds to optically thin dust emission and computed the equivalent gas mass per pixel as:

$$M_{\rm Gas} = \frac{R_{\rm gd} S_{250} D^2}{\kappa_{250} B_{250}\,(T_{\rm d})} \quad (2)$$

(Hildebrand 1983), where S_{250} is the 250 μm flux density within Ω, R_{gd} is the gas-to-dust mass ratio and κ_{250} is the dust absorption cross-section divided by the dust mass. We adopt R_{gd}/κ_{250}=25 gr cm^{-2}, computed from grain properties taken from Draine's tabulations (Li & Draine 2001, and references therein) for a grain size distribution that leads to a A_V/N_H ratio compatible with observations of Orion (see Section 3.2).

3. RESULTS

3.1. *Global Morphology of the [C II] 158μm Emission*

Figure 1 (left) shows a composite image of OMC 1 in the integrated line emission of CO 2-1 (red), [C II] 158 μm (blue) and H41α (green). This image shows the H II/PDR/molecular gas stratification expected in molecular clouds irradiated by strong UV fields from nearby massive stars.

The H41α recombination line traces dense ionized gas from the blister H II region surrounding the Trapezium. The H41α line peaks near the OB stellar cluster and is also bright adjacent to the Orion Bar PDR. Despite the different angular resolutions, the H41α emission morphology is similar to the brightest regions seen in the visible-light Hα images of the Orion Nebula (M42) (Figure 2 *left*; Robberto et al. 2013).

Figure 3 shows [C II], CO 2-1 and H41α spectra extracted from representative lines of sight toward OMC 1, namely the northern streamer, BN/KL, the Trapezium, the Orion Bar, the East PDR, and the extended cloud face in the south. OMC 1 has an overall face-on geometry, with the molecular cloud located ~0.3-0.6 pc behind the ionizing stars (e.g., Hogerheijde et al. 1995; van der Werf et al. 2013). Therefore, the observed ~10-15 km s^{-1} blue-shift of the H41α line relative to the [C II] and CO lines (Figure 3) is consistent with streamers of ionized gas escaping from the high-pressure H II/OMC 1 interface and moving toward the observer (e.g., Genzel & Stutzki 1989).

The regions of brightest [C II] 158 μm emission delineate the far edges of the H II blister and follow a roughly spherical shell distribution (as projected in the plane of the sky) with emission peaks near the Trapezium, at the east of BN/KL (that we refer to as the "East PDR") and along the Orion Bar PDR (Figure 1 right). These "interface" regions show very bright [C II] emission, with main beam temperature peaks of $\gtrsim$150 K (or a surface brightness of $\gtrsim$5×10^{-3} erg s^{-1} cm^{-2} sr^{-1} for the average Δv≃5 km s^{-1} line-width, see Figure 3). In addition, a more extended component of fainter [C II] 158 μm emission exists. In particular, the average line peak temperature in the map is ~70 K. This reflects the presence of a lower density and cooler component, the extended FUV-illuminated "face" of OMC 1 previously detected in [C II] at lower angular and spectral resolutions (Stacey et al. 1993; Herrmann et al. 1997). This extended component is also seen in the wide-field images of M42 taken in the emission from other low ionization potential (<13.6 eV) atoms (see the reddish nebular emission in Figure 2 taken with the [S II] filter in the visible). It is also seen in the near-IR vibrationally excited H_2 emission attributed to large-scale FUV fluorescence (Luhman et al. 1994).

Most of the [C II] (and obviously CO) emission is expected to arise from the neutral cloud. This can be readily seen from the similar [C II] 158 μm and CO 2-1 line profiles and also similar line peak velocities (Figure 3). At the small spatial scales revealed by our observations (~5000 AU), however, both the integrated intensity map (Figure 1 left) and the velocity channel maps (Figure 7) show that the [C II] and CO 2-1 spatial distribution does not exactly match. This is more obvious toward (nearly) edge-on PDRs, like the Orion Bar, because the irradiated cloud edge (emitting [C II]) can be resolved from the more shielded molecular gas, where CO reaches its abundance peak ($A_V \gtrsim 3$ mag for dense gas and strong FUV fields, see the representative model in Fig. 5).

The integrated intensity maps also reveal regions of moderately bright [C II] 158 μm emission, but very weak CO emission counterpart (northeastern areas). In addition, they show regions, such as the shocked gas toward H_2 Peaks 1 and 2 in Orion BN/KL outflows, where the CO line luminosities are exceptionally high (see also Goicoechea et al. 2015).

Finally, Figure 4 shows the good spatial correspondence between the [C II] 158 μm integrated intensity (contours) and the *Spitzer*/IRAC 8 μm emission (e.g., Megeath et al. 2012). This image is dominated by fluorescent IR emission from PAHs (after absorption of UV photons, e.g., Allamandola et al. 1989) and by very small grain emission, with minor contribution from [Ar III] toward the H II region and from H_2 lines toward particular positions of enhanced shocked gas emission (Rosenthal et al. 2000).

3.2. *Template Regions and Representative PDR Model*

Based on our knowledge of Orion (e.g., Genzel & Stutzki 1989; Stacey et al. 1993; Bally 2008), and in order to ease the interpretation of the [C II] and related maps, we introduce three different *template* regions (or sightlines). We first consider a 200″ (0.4 pc) radius circle centered on θ^1 Ori C, the brightest star of the Trapezium (e.g., the white dotted circle shown in Figure 4). We define the "extended cloud face" component for positions outside this circle. Secondly, a small R<0.1 pc circle around the Trapezium defines lines of sight that go through the "H II region" component around the H41α emission peak. Finally, we consider a spherical shell, or annulus, delineated by the R=0.16 pc and R=0.24 pc circles. This region represents "PDR interfaces" between OMC 1 and the H II region. These PDRs (specially the Bar) show a more edge-on configuration and are illuminated by the strong, almost unattenuated, UV field from the Trapezium stars.

To guide our interpretation, Figure 5 shows the predicted structure of the H/H_2 and C^+/C/CO transitions as a function of visual extinction (A_V) for physical conditions (G_0=2×10^4 and n_H=2×10^5 cm^{-3}) representative of the H II/OMC 1 interface near the

Trapezium (see Section 4). This homogeneous, stationary slab cloud model was computed with the *Meudon* PDR code (Le Petit et al. 2006). We adopted [C/H]=1.4×10^{-4} (from *HST* absorption observations towards the star HD 37021 in the Trapezium, Sofia et al. 2004) and a flat extinction curve compatible with observations of Orion (Lee 1968; Cardelli et al. 1989; Allers et al. 2005; Abel et al. 2006b). In particular, an extinction to color index ratio ($R_V = A_V/E_{B-V}$) of 5.5, and A_V/N_H=3.5×10^{-22} mag cm^{-} were adopted. These values are different than the standard grain properties used in diffuse cloud models (R_V = 3.1 and A_V/N_H=5.3×10^{-22} mag cm^{-2}) and are consistent with larger than standard size grains in Orion. Larger grains lead to an increased penetration of FUV photons, larger size of the C^+ zone ($\Delta A_V(C^+)\gtrsim1$ mag), higher C^+ column densities, and shift the peak CO formation layer to larger A_V deeper inside the cloud (see also Goicoechea & Le Bourlot 2007).

More in general, an ionization front can move into the molecular cloud. Ionized gas will rapidly photoevaporate from the cloud surface and the PDR structure will not be in equilibrium (e.g., Bertoldi & Draine 1996). Thus, dynamical effects might alter the picture shown in Figure 5. Non-stationary PDR models predict that a well defined C^+/CO transition layer always exists, although the layer is slightly shifted closer to the cloud surface (by only $\Delta A_V\simeq0.5$ for G_0/n_H conditions appropriate to OMC 1) due to advection of CO from inside the cloud (Störzer & Hollenbach 1998). Since the predicted C^+ column density in these models does not vary much compared to that in stationary models, the general predictions shown in Figure 5 for C^+ should remain valid.

3.3. *Kinematics: [C II] 158 μm Velocity Channel Maps*

Figures 6 and 7 show continuum-subtracted [C II] 158 μm velocity channel maps compared to those of H41α and CO 2-1 lines respectively. Both figures show the emission in 1 km s^{-1} velocity channels from v_{LSR} = −9 to +20 km s^{-1} ([C II] 158 μm in colored maps and H41α or CO 2-1 lines in white contours). They reveal the intricate small spatial-scale kinematics of the ionized/PDR/molecular gas interfaces.

The velocity-centroid of the molecular cloud emission[8], traced by CO, lies at $v_{LSR}\simeq$+(8-10) km s^{-1}. The [C II] 158 μm spectrum average over all mapped positions is characterized by a very bright component peaking at $v_{LSR}\simeq$ +9.5 km s^{-1}, with a line-width of ~5 km s^{-1} (lowest panel in Figure 3), in agreement with CO velocity and line widths.

This emission mostly arises from the H II/OMC 1 interfaces close to the Trapezium (inside the 200″ radius circle) and also from the large-scale FUV-illuminated face of the molecular cloud (outside). Therefore, *the main [C II] spectral component that coincides with CO (v_{LSR}~5-17 km s^{-1}) is dominated by C^+ in dense PDR gas and represents ~85 % of the total* [C II] *luminosity in the map*. The emission is so bright that the [^{13}C II] *F*=2-1 line, the strongest [^{13}C II] hyperfine component (Ossenkopf et al. 2013), is also detected toward the highest column density peaks (see the inset in Figure 3 and the channel maps between +17 and +20 km s^{-1} in Figures 6 and 7).

Other specific regions such as the Orion Bar PDR show [C II] line peak velocities at $v_{LSR}\simeq$ +(10-12) km s^{-1} and thus have a slightly differentiated kinematics. In fact, [C II] shows widespread emission in a broad range of velocities outside the main spectral component range. On the other hand, the CO 2-1 emission range is much more restricted, with the high velocity CO emission seen at v_{LSR}<0 km s^{-1} and v_{LSR}>15 km s^{-1} being very localized, and mostly arising from the molecular outflows surrounding Orion BN/KL and S.

Despite the relatively flat [C II] intensity distribution suggested by previous lower resolution observations, the [C II] channel maps show complicated structures and velocity patterns. This is true even away from the Trapezium, where filamentary structures and emission striations are seen at several velocity intervals. At the v_{LSR} ≈+8-10 km s^{-1} velocity of the neutral cloud, the H41α emission delineates the far edges of the expanding H II blister in close interaction with the cloud. This produces a bright shell-shaped [C II] emission from compressed PDRs immediately beyond the ionization fronts. This is the signature of the UV radiation *eating into* the cloud.

Also at v_{LSR} ≈+8-10 km s^{-1}, but away from the H II region, [C II] shows narrow striations or sheet-like structures that are roughly perpendicular to the main molecular ridge (north-to-south) and do not show much CO emission. As suggested by the overlap with the visible-light images of M42 (Figure 2), these photoevaporative [C II] structures demonstrate that the entire field and velocity range is permeated by FUV photons.

The most negative velocities show H41α emission around the Trapezium. This is probably the edge of the H II blister that is expanding toward the observer. The analogous [C II] emission has some spatial correspondence but it also shows specific blue-shifted structures that do not follow the H41α emission and that must lie in the line of sight toward OMC 1.

3.3.1. *C^+ Gas with no CO Counterpart*—In certain velocity ranges the observed [C II] emission does not have any CO emission counterpart. The most outstanding structure with no, or very little, CO emission is a blue-shifted [C II] emission "streamer" (v_{LSR}=−2 to +5 km $^{-1}$) that goes north of Orion BN/KL and also a compact region that fills the cavity inside the bright [C II] shell-like structure (Figure 2). These structures are not coincident with H41α emission tracing H II gas, suggesting that they arise from warm neutral gas of low shielding (A_V≈0-4 mag), in which very little or no CO exists (due to the elevated FUV field in the region and thus rapid photodissociation). Interestingly, they do coincide with foreground depressions of the visible-light emission known as the *Dark Bay* and the *Northern Dark Lane* that separates M42 and M43 nebulae (blue contours in Figure 2 *right*).

The column density of material in these structures is sufficient to have significant hydrogen in molecular form (consistent with the detection of radio OH lines in absorption toward the Dark Bay region, e.g., Brogan et al. 2005). Hence, they can be referred to *CO-dark H_2 gas* (Grenier et al. 2005; Wolfire et al. 2010), which can also be detected by dust extinction of visible light (O'Dell & Yusef-Zadeh 2000). In [C II] emission, they represent large-scale structures of C^+ gas surrounding OMC 1 and showing blue-shifted velocities relative to the molecular cloud (dark blue contours in Figure 2 right). In terms of luminosity, the [C II] emission from v_{LSR} ≃ −2 to +5 km s^{-1}, not related to OMC 1, accounts for ~12% of the total [C II] luminosity.

Europe PMC Funders Author Manuscripts

Surprisingly, the [C II] line shows emission components at even more negative LSR velocities throughout the region, in particular in the $v_{LSR} \simeq -10$ to -2 km s^{-1} range, and a fainter blue emission wing at $v_{LSR} \simeq -25$ to -10 km s^{-3}). (see spectra in Figure 3). Their combined contribution to the total [C II] luminosity is however small, ~3%.

Some of the structures showing [C II] emission but no CO counterpart can be associated, both spatially and in velocity space, with particular regions of H I absorption observed against the radio continuum. They are produced by the "Veil", a collection of absorbing H I layers in the line of sight toward Orion with little H_2, less than one part in 10^6 (Troland et al. 1989; Abel et al. 2006b). For a detailed explanation of the different H I absorbing velocity components (A, B, C, D …) see e.g., van der Werf et al. (2013). In particular, components A and B of the H I *absorption* maps, produce strong H I opacity in the $v_{LSR} \simeq 0$ to +6 km s^{-1} range. Components A and B are interpreted as a foreground veil of nearly atomic gas in front of the Orion nebula. Thus the [C II] emission in the $v_{LSR} \simeq 0$ to +6 km s^{-1} range, and outside the Dark Bay and North Dark lane regions, likely arises from these neutral atomic layers of the Veil (cyan contours in Figure 2 right).

Component C of the H I absorption (from $v_{LSR} \simeq -4$ to -2 km s^{-1}) is only found at the southwestern edge of OMC 1 and we also detect [C II] emission at those velocities and positions. Finally, H I absorption components D1 and D2 near the Bar appear in the $v_{LSR} \simeq -20$ to -10 km s^{-1} range and are interpreted as an expanding shell of atomic gas (van der Werf et al. 2013). The most blue-shifted [C II] emission ($v_{LSR} < -10$ km s^{-1}) is detected toward the southern regions of the map. Hence, part of this [C II] emission may arise from D1 and D2. In addition, a fraction of this blue-shifted [C II] emission may arise from the foreground H II region that lies between the Veil and the Trapezium, and that is not the main H II region interacting with OMC 1. [N II] λ6585Å emission line, and P III λ1335Å and S III λ1190Å absorption lines centered at $v_{LSR} < -13$ km s^{-1} arise from this foreground H II region (e.g., Abel et al. 2006b). Unfortunately, the sensitivity of our [C II] observations is insufficient to map these faint features and to determine a definite association.

H I *emission* tracing denser gas associated with the molecular cloud is detected at $v_{LSR} > +10$ km s^{-1}, outside the strong H I absorption range of the Veil. Indeed, we find specific regions that show coincident [C II] and H I red-shifted emission. The brightest one is the Orion Bar, where both [C II] and H I trace the most exposed PDR layers, in which H_2 is photodissociated. In addition, an elongated [C II] and H I emission feature without CO counterpart ($v_{LSR} \gtrsim +12$ km s^{-1}) extends in the southwest direction beyond the Bar and along the Bar prolongation seen at visible wavelengths (Figure 2). Another remarkable emission feature is the high-velocity [C II] and H I line-wing detected toward Orion BN/KL outflows. Its presence confirms that the shocked material is illuminated by FUV radiation (Chen et al. 2014; Goicoechea et al. 2015).

All in all, our observations demonstrate the link between [C II] and both H I absorption (hydrogen mostly atomic gas) and H I emission (hydrogen predominantly molecular). In particular, ~15% of the total [C II] luminosity does not have a CO counterpart. Most arises from cold H I gas and from CO-dark H_2 gas (e.g., the Dark Bay), but also from H II gas. The contribution from ionized gas is expected to decrease with increasing electron density (n_e)

Europe PMC Funders Author Manuscripts

and effective temperature (T_{eff}) of the ionizing stars (as carbon becomes doubly ionized). Both quantities are high toward the Trapezium, $T_{eff}\simeq$39,000 K for θ^1 Ori C star (Simón-Díaz et al. 2006), and $< n_e > \simeq (0.5\text{-}1)\times10^4$ cm^{-3} in the surrounding H II region (Zuckerman 1973). For these conditions, models predict that the contribution of [C II] from ionized gas is small, of the order of $\lesssim$10% of the PDR plus H II emission (Abel 2006a). This agrees with our general conclusion that most of the observed [C II] luminosity in Orion arises from dense PDR gas.

3.3.2. *[C II] Line Broadening and C⁺ Gas Turbulence*—The [C II] 158 μm line-width of the main spectral component varies between Δv_{FHWM}~3.5 km s^{-1} toward the extended "face" of OMC1, ~4.0 km s^{-1} toward the Orion Bar, and ~5.5 km s^{-1} toward the Trapezium. The two latter values are likely affected by opacity broadening (see Section 4.1 for a determination of [C II] opacities). In particular, for $\tau_{[CII]}\simeq$1-3, opacity broadening increases the line widths by ~10-30% (e.g., Phillips et al. 1979; Ossenkopf et al. 2013). We note that the line widths of the C91α radio recombination line toward the Orion Bar are 2.0-2.5 km s^{-1} (Wyrowski et al. 1997).

In the dense PDR gas traced by the [C II] main spectral component inside the 200″ radius circle, the gas temperature is $T_k\simeq$300-1000 K (see Figure 5 and Section 4.1.1), implying a thermal broadening of $\sigma_{th}=(k\,T_k/m_{C^+})^{1/2}\simeq$0.5-0.8 km s^{-1}. The nonthermal velocity dispersion σ_{turb} (from turbulence and macroscopic motions) is $\sigma_{turb}=(\sigma^2-\sigma_{th}^2)^2$ where $\sigma=\Delta v_{FHWM}/2.355$. For the above line-widths and gas temperatures, one obtains σ_{turb}=1.2-1.7 km s^{-1} turb (after opacity broadening correction). This has to be compared with the isothermal sound speed in the warm PDR gas, $c_{PDR}=(k\,T_k/m)^{1/2}\simeq$1.4-3.0 km s^{-1} (with m the mean mass per atom). In other words, the nonthermal velocity dispersion in the dense PDR gas is subsonic or only weakly supersonic (with Mach numbers σ_{turb}/c_{PDR} of $\simeq$0.4-1.2).

In the intermediate v_{LSR}=−2 to +5 km $^{-1}$ components, the [C II] line is narrower, for example Δv_{FHWM}~2.5-3.0 km s^{-1} toward the blue-shifted streamer that coincides with the North-Dark-Lane. On the other hand, the most blue-shifted [C II] component with neither CO nor H41α counterpart, for example the features at $v_{LSR}\simeq$−7 km s^{-1} toward (−150″,−300″) or at $v_{LSR}\simeq$−5 km s^{-1} toward (−37″, 274″), show again broader line-widths of Δv_{FHWM}~4.7−km s^{-1} (Figure 3). Assuming optically thin [C II] emission and T_k<300 K, we find an increased $\sigma_{turb}\simeq$2 km s^{-1} (or σ_{turb}/c_{HI}>2) in these CO-*dark* components surrounding OMC 1. These results suggest that the gas turbulence is more strongly dissipated in the dense H II/OMC 1 interfaces than in the surrounding, more turbulent, halo components.

3.4. *Surface Luminosity Maps*

Figure 8 shows maps of different luminosity[9] and luminosity ratios that are often discussed in the context of star formation and galaxy properties (e.g., Carilli & Walter 2013).

3.4.1. *Dust Opacity, Mass and Surface Density*—Figure 8(a) shows a map of L_{FIR} per pixel obtained by integrating the dust SED[6] fits at each position. Despite the relatively small area covered (~1.25 pc^2), the FIR intensity exhibits variations of ~3 orders of

Europe PMC Funders Author Manuscripts

magnitude (excluding Orion BN/KL). $L_{\rm FIR}$ is obviously high toward the high column density[10] regions in the molecular ridge ($N_{\rm H} \gtrsim 10^{23}$ cm^{-2}) and locally, it reaches even higher values toward the embedded star forming cores in Orion BN/KL. Figure 8(f) shows a map of the dust opacity ($\tau_{\rm d,160}$) from Equation (1) for each line of sight. The observations reveal moderate FIR opacities toward Orion S and along the molecular ridge ($\tau_{\rm d,160} \approx 0.2$). The FIR opacity then decreases from the Bar ($\tau_{\rm d,160} \lesssim 0.1$) to the extended regions ($\tau_{\rm d,160} \approx 0.01$). Note that the 160 μm dust emission toward Orion BN/KL is optically thick ($\tau_{\rm d,160}$>1, Goicoechea et al. 2015, and Sect. 5.4.1).

The total gas mass in the mapped region is computed from the optically thin dust emission at 250 μm using Equation (2). For the assumed grain properties (see Section 3.2), we derive $M_{\rm Gas,Total} \simeq 2600\ M_{\odot}$ in the ~0.9 pc ×1.4 pc mapped area (excluding Orion BN/KL that adds ~100 × $M_{\odot}$; Goicoechea et al. 2015). This is equivalent to a surface density of $\Sigma_{\rm Gas}{\simeq}2000\ M_{\odot}$ pc^{-2}. We note that a $R_{\rm gd}/\kappa_{250}$ ratio higher than the assumed in this work will increase our gas mass estimate and the $N_{\rm H}$-to-A_V conversion value accordingly. Unfortunately, the exact grain composition and optical properties in molecular clouds like OMC 1 are not fully constrained (Goldsmith et al. 1997), and they likely change on small scales (Arab et al. 2012). Owing to the similar gas masses reported from large-scale ^{13}CO and submm continuum mapping (Bally et al. 1987; Lis et al. 1998; Berné et al. 2014), we estimate that our $M_{\rm Gas}$ and $N_{\rm H}$ values are uncertain by a factor of $\lesssim$2.

3.4.2. *L*[C II]/*L*$_{\rm FIR}$ and *L*[C II]/*L*$_{\rm CO\ 2-1}$ Maps—Figure 8(d) shows the spatial distribution of the L[C II]/$L_{\rm FIR}$ luminosity ratio toward OMC 1. L[C II]/$L_{\rm FIR}$ varies from the more extended and translucent cloud component, where $N_{\rm H} \simeq 10^{21-22}$ cm^{-2} and L[C II] carries up to ~1-5 % of the FIR luminosity, to the dense molecular ridge, where $N_{\rm H} \simeq 10^{24}$ cm^{-2} and L[C II] only carries ~0.01%. The mean (median) value in the map is L[C II]/$L_{\rm FIR}$ = 3.8 (2.9) × 10^{-3}. This is similar to the value observed toward translucent clouds of the Galaxy (Ingalls et al. 2002). Indeed, low angular resolution surveys of the Milky Way show that the typical L[C II]/$L_{\rm FIR}$ ratio in regions of weak [C II] emission is ~4×10^{-3}, and decreases to ~10^{-3} toward star-forming regions where the [C II] line is brighter (e.g., Nakagawa et al. 1998).

The $L_{\rm FIR}$ map per pixel in Figure 8(a) can be used to estimate, to first order, the spatial distribution of G_0. Assuming that at large scales the entire column density of dust is heated by absorption of FUV photons, dust grains re-radiate in the FIR at a characteristic temperature ($\approx T_{\rm d}$) and;

$$G_0 \approx \frac{1}{2}\frac{I_{\rm FIR}\,({\rm erg\ \ s^{-1}\,cm^{-2}\,sr^{-1}})}{1.3\times10^{-4}}, \quad (3)$$

(see Hollenbach & Tielens 1999) where G_0 is the FUV field in Habing units[11]. The factor of 1/2 approximately takes into account the absorption of visible photons by dust. The maximum value near the Trapezium is $G_0{\simeq}10^5$, whereas the lowest values in the mapped area are G_0>500. The mean value inside the 200″ radius circle is $G_0{\simeq}2{\times}10^4$ (the G_0 used in the representative PDR models shown in Figure 5). These FUV fluxes are in good agreement with early estimates based on lower angular resolution observations and PDR modelling (e.g., Tielens & Hollenbach 1985b; Stacey et al. 1993).

The [C II] and CO 2-1 luminosities in the observed area are L[C II]=173 $L_\odot$ and $L_{CO\ 2-1}$=0.15 $L_\odot$. Figure 8(e) shows the L[C II]/$L_{CO\ 2-1}$ map. The spatial distribution is markedly different from that of L[C II]/L_{FIR}. In particular, the L[C II]/$L_{CO\ 2-1}$ ratio shows differences locally, from a few hundred in the strong outflows around Orion BN/KL, to ~5000 in the peculiar northeastern positions almost devoid of CO emission (see white marks in the $L_{CO\ 2-1}$ map shown in Figure 8(c)). At other positions of the map, the ratio reaches high values (>1000), either because the observations trace regions of low extinction (i.e., low CO columns) or nearly edge-on PDRs for which the C^+/CO transition is spatially resolved. Table 2 summarizes the mean values extracted from the maps toward the different regions of the cloud.

4. ANALYSIS

4.1. *[C II] 158 μm Excitation and C+ Column Densities*

Collisions with electrons, H atoms and H_2 molecules contribute to the excitation of the [C II] $^2P_{3/2}$-$^2P_{1/2}$ fine structure levels (see discussion by Goldsmith et al. 2012). The critical densities (n_{cr}) for collisions of C^+ with, e, H and H_2 are ~44 e / cm^3 at T_e=8000 K (Wilson & Bell 2002), and ~3000 (2400) H/ cm^3 (Barinovs et al. 2005) and ~4500 (3400) H_2 / cm^3 at T_k = 100 (500) K (Wiesenfeld & Goldsmith 2014). Owing to the similar collisional rates with H_2 and H, the [C II] excitation in neutral gas is nearly independent of the molecular fraction. As the gas density increases above n_{cr}, the excitation temperature T_{ex} of the $^2P_{3/2}$-$^2P_{1/2}$ transition tends to thermalize with T_k. For optically thick lines, line-trapping further reduces the critical densities, thus reaching thermalization (T_{ex}=T_k) at lower densities. Also for optically thick lines, a strong FIR background with high T_{bg} values increases T_{ex} but reduces the [C II] line intensity.

When $n_H \lesssim n_{cr}$, the [C II] excitation becomes sub-thermal ($T_{ex} < T_k$). If significant C^+ columns of low-density gas exist in front of a FIR continuum source, the [C II] line will be seen in absorption if $T_{ex} < \frac{91.2}{ln\,(1+91.2/T_c)}$ (e.g., Gerin et al. 2015), where $h\nu/k$ = 91.26 K is the equivalent temperature at 1900.537 GHz, and $T_c = J\,(T_{bg}) = \frac{91.2}{e^{9.12/T_{bg}}-1}$ is the continuum brightness temperature at 158 μm. [C II] line self-absorptions can also be produced by excitation gradients within the [C II] emitting region (e.g., Plume et al. 2004; Graf et al. 2012).

One potential problem in interpreting the [C II] 158 μm emission is the difficulty inferring the line opacity. Toward many positions, our observations resolve the [^{13}C II] F=2-1 line[12] arising from the main spectral component at $v_{LSR} \simeq$ +9.5 km s^{-1} (see spectra in Figure 3 and maps in the highest-velocity panels of Figures 6 and 7). The second brightest component, the [^{13}C II] F=1-0 line, is only detected toward a few positions of very bright [C II] emission (e.g. the Orion Bar and BN/KL, see Figure 3). Assuming that the total integrated intensity of the three [^{13}C II] lines is I[^{13}C II] = $I_{F=2-1}$/0.625, one can derive the [C II] line opacity from[13]:

$$\frac{1-e^{-\tau_{[\mathrm{CII}]}}}{\tau_{[\mathrm{CII}]}} \simeq \frac{0.625 T_{\mathrm{P}}\left(\left[{ }^{12} \mathrm{CII}\right]\right) / T_{\mathrm{P}}\left(\left[{ }^{13} \mathrm{CII}\right], F=2-1\right)}{\left[{ }^{12} \mathrm{C} /{ }^{13} \mathrm{C}\right]} \quad (4)$$

(e.g., Ossenkopf et al. 2013) where $\tau_{[CII]}$ is the [C II] 158 μm opacity at line center, T_P is the line peak main beam temperature (continuum-subtracted) and [^{12}C/^{13}C] is the isotopic ratio (~67 in Orion, Langer & Penzias 1990). For optically thick [C II] 158 μm emission, the excitation temperature (T_{ex}) of the $^2P_{3/2} - P_{1/2}$ transition can be computed from:

$$T_{\mathrm{ex}}=\frac{91.2}{\ln\left(1+\frac{91.2}{T_{\mathrm{P}}\left({ }^{12} \mathrm{C}^{+}\right)+J\left(T_{\mathrm{bg}}\right)}\right)}\ (\mathrm{K}) . \quad (5)$$

At these FIR wavelengths, the background is dominated by dust emission so that the continuum level adjacent to the [C II] line, for an equivalent background temperature of 20 – 35 K, is $T_c = 1 - 7$ K, roughly the range of continuum levels detected by HIFI. For the main [C II] 158 μm spectral component we find $T_P(^{12}C^+) \gg T_c$, thus the continuum emission has a minor effect on T_{ex}. However, the situation can be different in more extreme and luminous environments.

Once T_{ex} ($^2P_{3/2} - P_{1/2}$) and $\tau_{[CII]}$ have been determined, the C^+ column density can be computed from:

$$N\left(\mathrm{C}^{+}\right) \simeq 1.5 \times 10^{17} \frac{1+2 e^{-91.2 / T_{\mathrm{ex}}}}{1-e^{-91.2 / T_{\mathrm{ex}}}} \tau_{[\mathrm{CII}]} \cdot \Delta \mathrm{v}_{\mathrm{FWHM}} \quad \left(cm^{-2}\right) \quad (6)$$

where Δv_{FWHM} is the line width in km s^{-1} of an assumed Gaussian line-profile. From the [C II] and [^{13}C II] spectra averaged over the mapped region (main spectral component) we find < T_{ex} >≃ 100 K, < $\tau_{[CII]}$ >≃ 1.3 and < $N(C^+)$ >≃ 3 × 10^{18} cm^{-2}. The highest C^+ column density peaks are found near the Trapezium, the Orion Bar, the East PDR and northeast of Orion BN/KL. In these emission peaks, the excitation temperatures and line opacities (T_{ex} = 250 – 300 K and $\tau_{[CII]} \simeq 1 - 2$) are higher than the average. The 25″ beam-averaged C^+ column density toward these peaks is $N(C^+) \simeq 10^{19}$ cm^{-2}.

The inferred excitation temperatures can be used to further constrain *the origin of the [C II] emission at the FUV-illuminated surface of the molecular cloud*. In particular, the mean $T_{ex} \gtrsim 100$ K values inferred from the map require the fractional population of the $^2P_{3/2}$ level, $n(^2P_{3/2})/n(^2P_{1/2}+^2P_{3/2})$, to be >0.45. The representative PDR model in Figure 5 shows that the conditions for producing significant [C II] emission are quite restrictive. For high FUV radiation fields, the C^+ layers extend to $A_V \simeq 3$-4 mag but the gas temperature falls much faster for any reasonable density. Figure 5 shows that a fractional population >0.45 of the $^2P_{3/2}$ level requires high gas densities ($n_H \simeq 5 \times 10^3$ for even $T_k \simeq 500$ K, see Figure 10). Hence, the bright [C II] emission from OMC 1 traces narrow cloud surface layers (A_V<4 mag) and not the entire line of sight.

In the extended regions, the [^{13}C II] lines are not detected and the [C II] 158 μm line is weaker. This suggests that the line is optically thin or *effectively* thin (Goldsmith et al.

2012). The line opacity can be derived if one knows T_{ex}. Here we make the approximation $\tau_{[CII]} \simeq T_P([C\,II])/J(T_{ex})$. Figure 9(a) shows a column density map, computed under these assumptions, of the blue-shifted component (v_{LSR}≃−2 to +5 km s^{-1}) that includes the Dark Bay and the Northern Dark Lane emission. We adopted a constant T_{ex}≃80 K (intermediate between T_k in the OMC 1/H II interfaces and that in the atomic Veil (Abel et al. 2009). The resulting $N(C^+)$ toward the Dark Bay (≃1.4×10^{18} cm^{-2}) is equivalent to $A_V \simeq N(C^+)/4\times10^{17}$≃3.5 mag (i.e., significant H_2 must be present) assuming that the bulk of the gas-phase carbon is in C^+, with an abundance of 1.4×10^{-4} (Sofia et al. 2004). This value is consistent with the extinction peak determined toward the Dark Bay (O'Dell & Yusef-Zadeh 2000). Other sightlines with $N(C^+)<8\times10^{17}$ cm^{-2} (A_V<2 mag) are likely associated with C^+ in nearly atomic H I gas (e.g., toward the Traprezium). The integrated C^+ column density in the map (v_{LSR}≃−2 to +5 km s^{-1} component) is compatible with the observed [C II] fractional luminosity of ~12% (Section 3.3).

In addition, Figure 9(b) shows a $N(C^+)$ map of the OMC 1 component (v_{LSR}≃5 to +17 km s^{-1}) adopting T_{ex}≃100 K from the map averaged spectrum. Figure 9(c) shows the resulting map of the total C^+ column density along each line of sight, $N(C^+)^{Total}=N(C^+)^{OMC1}+N(C^+)^{blue}+N(C^+)^{<-2km/s}$, where we have added, at each position, $N(C^+)^{<-2km/s}=10^{17}$ cm^{-2} from additional foreground emission components at v_{LSR}<−2 km s^{-1}. The integrated column density in the <−2 km s^{-1} component is consistent with the 3% contribution to the total [C II] luminosity. This is equivalent to $A_V^{<-2km/s} \simeq 0.25$ mag (i.e., fully atomic or ionized gas). We finally note that along many sightlines, the C^+ column in the Veil is comparable to that computed in the OMC 1 surface. In these approximate maps of the C^+ components without CO counterpart, ~30 % of the C^+ mass is in CO-dark H_2 gas.

Figure 9(d) shows the $N_{\rm H}^{\rm Total}$ column density map obtained from the dust emission[10]. Both $N(C^+)^{Total}$ and $N_{\rm H}^{\rm Total}$ maps can be used to estimate the fraction (f) of the total column density traced by [C II] along each line of sight. In particular, Figure 9(e) shows the distribution of the $f=[N(C^+)/N_H]/1.4\times10^{-4}$ ratio at 25″ resolution. Note that this map is similar to the L[C II]/L_{FIR} map shown in Figure 8(d). The lowest values $f \ll 1$ are inferred toward the high N_H column density ridge (bluish regions with $f \lesssim$5 %). These fractions are consistent with the presence of a massive molecular cloud behind the [C II] emitting surfaces. The typical fractions outside the ridge are $f \simeq$20-30 % (greenish regions). Far from the Trapezium, toward the extended cloud component, fractions higher than $f \gtrsim$50 % are only inferred toward the most translucent lines of sight. The [C II] emission toward the dense PDRs around the Trapezium is slightly optically thick and T_{ex} is higher than the average value assumed in the f map. The corrected fraction using the column of $N(C^+)\simeq10^{19}$ cm^{-2} computed from [^{13}C II] is f≃40 %.

We also used the C^+ column map to compute the "PDR mass" in OMC 1. In particular, we integrate the equivalent $N_{H,PDR}=N(C^+)^{OMC1}/1.4\times10^{-4}$ column traced by [C II] as $M_{\rm PDR} \simeq \mu\, m_{\rm H} \sum_i \left(N^i_{\rm H,PDR}\, A_i\right)$, where A_i is the area of pixel i, m_H is the H atom mass and μ is the mean atomic weight. We derive M_{PDR}≃200 $M_\odot$, i.e., the PDR mass fraction traced by [C II] is ~8% (within a factor of ~2).

4.1.1. *[C ii] Radiative Transfer Models*—In order to constrain the range of physical conditions that reproduce the observed [C ii] 158 μm emission toward OMC 1, we have run a grid of non-local and non-LTE radiative transfer models of the $^2P_{3/2}$ –$^2P_{1/2}$ doublet that take into account line trapping and opacity broadening (see Appendix in Goicoechea et al. 2006). For consistency, we included illumination by a FIR background continuum field and a combined treatment of gas and dust emission/absorption. Hence, at a given wavelength the opacity is given by $\tau_\lambda = \tau_{[\mathrm{CII}]} + \tau^{local}_{d,160}$. We used a constant column density of $N(C^+)=3\times10^{18}$ cm^{-2}, the mean value we infer from the OMC 1 map, and a nonthermal velocity dispersion σ_{nth} = 1.3 km s^{-1} (see Sec. 3.3.2). The models use the latest available collisional rates of C^+ with *e*, H and H_2 (with a LTE H_2 ortho-to-para ratio at each T_k) and assume n_e = [C^+ /H] n_H = 1.4 × 10^{-4} n_H and n(H)=0.25 $n(H_2)$ (a molecular fraction, 2 $n(H_2)$/[n(H)+2 $n(H_2)$], of ≃0.9). For gas densities n_H=2×10^5 cm^{-3} and T_k=500 k, this choice of parameters implies that the [C ii] $^2P_{3/2}$-$^2P_{1/2}$ collisional rate is due to collisions with H_2 molecules (~70%), H atoms (~25%) and electrons (~5%). The FIR background radiation field is modelled as thermal emission at 30 K (roughly the mean dust temperature we derive from SED fits) and the temperature of the dust grains mixed with the C^+ atoms is set to 50 K (typical of highly illuminated PDRs at $A_V \approx 2$ mag).

Figure 10 shows model results in the form of iso-T_{ex} contours. The mean [C ii] excitation temperature in the *Herschel*/HIFI map is T_{ex}≃100 K. This plot shows that the minimum gas density required to produce this T_{ex}=100 K is n_H≃5×10^3 cm^{-3}. Toward the H ii /OMC 1 interfaces (the spherical shell of PDRs around the Trapezium) T_{ex} reaches higher values (~250-300 K). This sets a higher limit to the gas density of n_H10^5 cm^{-3} (including the Orion Bar). The more elevated temperatures in these dense PDRs (T_k ≳300 K) are consistent with the T_k=400-700 K values inferred from H_2 pure rotational lines (Allers et al. 2005) and with T_k≃540 K derived from H i emission, both measurements toward the Orion Bar PDR (van der Werf et al. 2013).

Finally, the presence of a foreground halo of low-excitation material can produce [C ii] absorption. Such a halo will also absorb or scatter the [C ii] line photons emitted inside the cloud, if the absorption is produced at similar velocities. This may be the case of components A and B of the H i absorption in the Veil. These components peak at v_{LSR}≃0-6 km s^{-1} (van der Werf et al. 2013) and coincide with the blue-wing of the [C ii] emission seen in the main spectral component. The gas temperature and density in components A and B of Orion's Veil are estimated from H i lines to T_k≃50-80 K and n(H)≃10$^{2.5-3.4}$ cm^{-3} (Troland et al. 1989; Abel et al. 2006b). For the FIR background in OMC 1 and for the parameters in our grid, we do predict [C ii] absorption for low excitation gas (white line in Figure 10). Hence, the [C ii] emission dips seen in some velocity intervals may be produced by [C ii] absorption in the Veil (e.g. toward the Orion Bar PDR at v_{LSR}≃+1 km s^{-1}, toward the southwest (−150″,−300″) position at v_{LSR}≃+3 km s^{-1} or toward the (−62″,250″) position in the northern streamer at v_{LSR}≃+6 km s^{-1}, see channel maps).

In any case, our [C ii] excitation models confirm that the gas density in the FUV-illuminated face of OMC 1 is high. The blue-shifted [C ii] emission caused by the Veil also shows that the density must be relatively high in these foreground components. This agrees with the

Europe PMC Funders Author Manuscripts

Europe PMC Funders Author Manuscripts

general notion that the elevated stellar density in the Orion cluster is a consequence of hundreds of stars that formed from a remarkably dense condensation (e.g., Genzel & Stutzki 1989; Rivilla et al. 2013).

4.2. *Correlation Diagrams*

Figure 11 shows correlation plots between several quantities that are also used in the discussion of the [C II] extragalactic emission (one point, one galaxy). Here we present their spatial correlation in a template massive star-forming region. In these plots, the black points represent positions outside the 200″ (0.4 pc) radius circle, the "extended cloud face" component. Green squares represent lines of sight toward the "H ii region" component around the Trapezium stars, and red triangles represent positions in the "dense PDR interface" annulus. Gray points are other positions inside the 200″ circle that do not fall in the latter two categories.

Figure 11(a) shows that the [C II]/FIR ratio decreases with increasing FIR intensity. In OMC 1 we find that log ([C II]/FIR)$\simeq$−0.6·log ($I_{\rm FIR}$[erg s^{-1} cm^{-2} sr^{-1}]) 2.6, with a correlation coefficient of ρ=−0.93. This is reminiscent of the "[C II] deficit" observed in local ULIRGs when compared to starburst and normal galaxies (e.g., Malhotra et al. 1997; Luhman et al. 1998; Graciá-Carpio et al. 2011). In a local complex like Orion, the decrease of L[C II]/$L_{\rm FIR}$ obviously occurs at orders of magnitude lower FIR luminosities and seems dominated by the strong variations of $I_{\rm FIR}$ in the region. The blue line in Fig. 11(a) shows a linear model for a constant [C II] intensity cloud (the median value of the map sample).

Figure 11(b) shows that $I_{\rm FIR}$ increases with $\tau_{\rm d,160}$. Figure 11(c) shows a L[C II]/$L_{\rm FIR}$-$T_{\rm d}$ scatter plot. In many studies, in which a complete SED cannot be constructed, $T_{\rm d}$ is replaced by the F_{60}/F_{100} or F_{70}/F_{160} flux ratio. Theoretical models show that the photoelectic heating efficiency decreases for high $G_0/n_{\rm H}$ values (also producing higher dust temperatures), because grains and PAHs get more positively charged and it becomes more difficult to photo-eject additional electrons (Tielens & Hollenbach 1985; Okada et al. 2013). As the grain charge increases for high G_0 fields, the gas heating and cooling are reduced and a larger fraction of the FUV field is converted into dust FIR luminosity (thus lower L[C II]/$L_{\rm FIR}$ ratios can be expected). Although such a trend is suggested by Figure 11(c), the dust temperatures obtained from the SED fits, $T_{\rm d}$=31×4 K (1σ), do not change much over the mapped region and other effects seem to dominate the observed L[C II]/$L_{\rm FIR}$ variations at large spatial scales.

In particular, most of the dust emission in the extended cloud is consistent with an roughly constant temperature of $T_d\simeq$30 K. This leads to the approximately linear relation between dust opacity and FIR intensity shown in Figure 11(b). However, the inferred dust temperatures toward some lines of sight of small $\tau_{\rm d,160}$ are lower than 30 K, resulting in lower $L_{\rm FIR}$ values than those expected in a constant T_d cloud (blue line Figure 11(b)), as well as in high L[C II]/$L_{\rm FIR}$ ratios in Figure 11(a). On the other hand, the dust is warmer toward the dense PDRs and H II region, and high $I_{\rm FIR}$ intensities are observed above the constant-T_d blue line in Figure 11 (b). The higher dust temperatures toward the central of OMC 1 likely reflect higher G_0 values and also contribution from internal dust heating by embedded sources. However, their associated L[C II]/$L_{\rm FIR}$ ratios lie above the linear model that assumes constant [C II] emission in Figure 11(a), revealing enhanced [C II] intensity toward these regions. Still, the FIR intensity increases more than [C II] (Figure 11(d)), and the resulting L[C II]/L_{FIR} ratios are low toward lines of sight of high dust temperatures, see Figure 11(c) and Section 5.4.1.

Figure 11(d) shows that, except for high FIR intensities, the [C II] 158 μm intensities are reasonably well correlated with the FIR emission (ρ=0.75), with $I_{[CII]}\simeq4.1\times10^{-4}\times I_{FIR}+2.2\times10^{-3}$ (in erg s^{-1} cm^{-2} sr^{-1} units). The [C II] intensities, however, are better correlated with the PAH emission traced by the IRAC 8 μm image (ρ=0.91, Figure 11(f)), with $I_{[CII]}\simeq2.6\times10^{-2}\cdot I_{IRAC\ 8\mu m}+1.6\times10^{-3}$ (also in erg s^{-1} cm^{-2} sr^{-1} units). As opposed to FIR, this correlation seems to hold for high [C II] and PAH intensities. Finally, Figure 11(e) shows a correlation plot of L[C II]/L_{FIR} with L_{FIR}/M_{Gas}. This plot shows much more scatter, but suggests that L[C II]/L_{FIR} decreases from the extended cloud to the “H II region” component (highest L_{FIR}/M_{Gas} values).

5. DISCUSSION

5.1. *[C II], CO and FIR Diagnostic Power*

Dense PDR models predict that the low-J ^{12}CO lines saturate ($\tau\gg1$) close to the CO abundance peak and thus the L[C II]/L_{CO} ratio depends mostly on N(C$^+$) and T_k, i.e., on G_0 and n_H (see e.g., PDR models by Kaufman et al. 1999). For densities below n_{cr}~10^4 cm^{-3} and $G_0<10^3$, the [C II] 158 μm line dominates the gas cooling (Kaufman et al. 1999) and the L[C II]/L_{FIR} ratio provides a good approximation to the grain photoelectric heating efficiency. For higher densities or G_0 values (i.e., the OMC 1/H II interfaces around the Trapezium), [C II] collisional de-excitation plays a role and [O I] starts to dominate the warm gas cooling. [O I] 63,145 μm lines are certainly useful (Herrmann et al. 1997) although they are also bright in dissociative shocks where the [C II] line is faint (e.g., Goicoechea et al. 2015). In addition, the opacity of the [O I] 63 μm line is higher ($\tau_{[OI]}=1.6\,\tau_{[CII]}$ for a [O/C]=2.2 abundance ratio) and lies at wavelengths of higher dust opacity (2.5-6.3 times higher for β=1-2). The [O I] 63 μm line opacity problem is difficult to circumvent, because ^{18}O does not have nuclear spin (producing hyperfine splittings in ^{13}C$^+$), and the isotopic shift with respect to ^{16}O is only ~1.5 km s^{-1} (+23.5 MHz, Brown et al. 1993). Therefore, [C II] is a robust tracer of the presence of FUV photons also in dense gas.

As noted in the literature, L[C II]/L_{FIR} approximately follows $L_{CO\ 2-1}/L_{FIR}$ (Figure 12). For most of the mapped positions, the observed luminosities appear well correlated (ρ=0.89 and slope of $\simeq$775). Stacey et al. (1991) suggested that, to a first approximation, the L[C II]/L_{FIR} and L_{CO}/L_{FIR} luminosity ratios can be compared with PDR models to constrain the FUV radiation field and the gas density. Most of the points in Figure 12 roughly lie on a straight line. In the frame of PDR models (e.g., Kaufman et al. 1999) this line approximately follows the decrease of G_0 (from left to right) and the decrease of n_H (from bottom to top). Comparing our spatially resolved luminosity ratios[14] (Figure 12) with the plot in Figure 5 of Stacey et al. (2010), based on PDR models of Kaufman et al. (1999) for a A_V=10 mag slab, one sees that the lowest L[C II]/$L_{FIR}\simeq3\times10^{-4}$ and $L_{CO\ 2-1}/L_{FIR}\simeq3\times10^{-6}$ values near the Trapezium are consistent with high $G_0\gtrsim10^4$ fields and $n_H\gtrsim10^5$ cm^{-3}. On the other hand, the highest L[C II]/$L_{FIR}\gtrsim10^{-2}$ values, corresponding to $L_{CO\ 2-1}/L_{FIR}\lesssim10^{-4}$ ratios in the extended cloud component are consistent with lower FUV fields and gas densities, G_0>10^2 and n_H≈10^{3-4} cm^{-3} respectively.

In addition, our maps reveal regions in which the luminosity ratios lie outside the parameter space allowed by A_V=10 mag PDR models (blue pentagons in Figure 12). These are specific positions with very high L[C II]/$L_{CO\ 2-1}$≃5000 luminosities and low $\tau_{d,160}$ opacities at the northeast of the map. Since they do not coincide with the H II region, we conclude that they must be associated with lower density neutral gas at low A_V (thus low CO abundances for $G_0 \gg 1$ values). Indeed, a much better match with PDR models is found by considering the A_V≃3 mag cloud models of Kaufman et al. (1999).

5.2. *[C II] and the Star Formation Rate in Orion*

Herschel/HIFI has allowed the first velocity-resolved [C II] survey of the Galactic plane, in which the contribution of the different ISM phases to the [C II] emission has been constrained (e.g., Pineda et al. 2013). The combined [C II] emission from all components added together correlates with the SFR in similar manner as in nearby galaxies. Including observations of the Milky Way, the LMC and several nearby galaxies dominated by star formation, Pineda et al. (2014) find: log (SFR [$M_\odot$ yr^{-1}])≃0.89 log (L[C II][erg s^{-1}])–36.3. Using this correlation and the total [C II] luminosity – toward OMC 1, we derive SFR≃3.8×10^{-5} $M_\odot$ yr^{-1} in the mapped area. This is very similar to the rate obtained using SFR($M_\odot$ yr^{-1})≃ L_{FIR}/5.8 10 observed × ^{9} $L_\odot$ (e.g., Kennicutt 1998) and the luminosity toward OMC 1 (L_{FIR}≃2×10^5 $L_\odot$).

In addition, extinction maps galactic star-forming regions suggest that the SFR correlates with the mass (M') of the UV-shielded (A_V≳7 mag) dense gas (n(H$_2$)>10^4 cm^{-3}), the reservoir that ultimately forms stars (e.g., André et al. 2010; Lada et al. 2010; 2012). These studies suggest SFR [$M_\odot$ yr^{-1}] ≃ (1.2-1.8)×10 ^{8} M' ($M_\odot$), and this corrrelation holds from star-forming regions to galaxies (Gao & Solomon 2004; Wu et al. 2005). Taking the masses inferred from our observations, we estimate M'≃$M_{Gas,Total}$–M_{PDR}≃2400 $M_\odot$ (using the total mass deduced from the dust emission and subtracting the PDR contribution inferred from [C II]), and use the above relation to derive SFR≃(2.9-4.3)×10^{-5} $M_\odot$ yr^{-1}. Therefore, the different methods provide consistent SFR values in Orion.

Taking into account the mapped area, our derived SFR is equivalent to a very high SFR surface density of $_{SFR}$=(2.3-3.4)×10^{-5} $M_\odot$ yr^{-1} pc^{-2}. Together with the high surface density inferred from the mass estimates (Σ_{Gas}≃2000 $M_\odot$ pc^{-2}), these values place the core of Orion at an extreme of a Kennicutt–Schmidt-type surface density relation ($\Sigma_{SFR} \propto \Sigma_{Gas}^{\alpha}$ with α close to 1). These, and even higher surface densities are also inferred toward luminous galaxy mergers hosting intense star formation (Genzel et al. 2010).

5.3. *L[C II]/L$_{FIR}$ Variations and Extragalactic Link*

The reduced L[C II]/L_{FIR} luminosity observed toward local ULIRGs (L_{FIR}≳10^{12} $L_\odot$) has been difficult to interpret. Dust extinction, optically thick [C II] emission, reduced photoelectric heating efficiency or soft UV fields from less massive stars have been invoked (e.g., Luhman et al. 1998). In addition, extragalactic observations with *Herschel* suggest that the “line deficit” (relative to L_{FIR} or $L_{\mathrm{FIR}}/M_{\mathrm{Gas}}$) also applies to other FIR fine structure lines such as [O I], [N II] or [O III] arising either from PDRs or H II regions (Graciá-Carpio et al. 2011).

The $L_{\mathrm{FIR}}/M_{\mathrm{Gas}}$ ratio in particular, is expected to be proportional to the ionization parameter U (the number of H ionizing photons, Q(H), divided by the density n_{H} and by the distance to the ionizing stars). The FIR line deficit becomes more apparent in galaxies with very high $L_{\mathrm{FIR}}/M_{\mathrm{Gas}} \gtrsim 80 L_{\odot} M_{\odot}^{-1}$ values (Graciá-Carpio et al. 2011; González-Alfonso et al. 2015). This threshold has been suggested to separate normal galaxies from ultra-luminous mergers characterized by very high SFRs (Genzel et al. 2010).

These authors suggest that the ISM conditions and the star-formation efficiency in these galaxies are different from those in normal and starburst galaxies. In this context, the FIR line deficits (including [C II]) would be explained by the much higher ionization parameters and more extreme conditions of the H II/PDR regions they host (e.g., Graciá-Carpio et al. 2011). Photoionization models including dust grains indeed predict reduced L[C II]/L_{FIR} values for high log $U > -2$ parameters (Abel et al. 2009). One of the predicted effects is that grains absorb a higher fraction of the available UV photons relative to the gas, leaving fewer photons to ionize and heat the gas. Models of the radiative pressure on grains do show that dusty H II regions have a different ionization balance and that they compress the gas and dust into a dense ionized shell (Draine 2011). This is very suggestive of the shell-like structure revealed by the [C II] and H41α emission around the Trapezium. On the other hand, Draine (2011) concludes that owing to the accumulation of gas and dust in a dense shell, the fraction of photons that ionize the gas actually increases (relative to a uniform H II region). In this context, the effects of increasing U may not be so severe.

Observational evidence for the presence of PAH and grains in H II regions is increasing (Ochsendorf & Tielens 2015). Their role in modulating the FUV field reaching the neutral cloud surface needs to be taken into account. The H II region around the Trapezium contains dust and is indeed characterized by a relatively high ionization parameter (log $U \simeq -1.48$ and Q(H)~10^{49} s^{-1}, Baldwin et al. 1991). The presence of grains in the ionized nebula can be inferred from the depleted abundances of refractory elements like Mg, Si and Fe from the gas phase (e.g., Simón-Díaz & Stasińska 2011).

In Orion, the sightlines with $L_{\mathrm{FIR}}/M_{\mathrm{Gas}} > 80 L_{\odot} M_{\odot}^{-1}$ show a very good spatial correspondence with the dense H II ionized gas traced by the H41α line and so they do trace regions of high ionization parameter (white thick contour in Figure 13) In particular, the highest $L_{\mathrm{FIR}}/M_{\mathrm{Gas}}$ ratios are observed close to the H41α emission peaks: the dense ionized gas toward the Trapezium cluster and also the ionization front that precedes the Orion Bar PDR. These regions are characterized by more extreme UV irradiation conditions ($G_0 > 10^4$).

We finally note that the luminosity of the large-scale vibrationally excited H_2 line emission toward OMC 1 is dominated by FUV-exited fluorescent emission in PDR gas (>98%, see Luhman et al. 1994) even though the collisionally excited (shocked) H_2 dominates the small-scale emission of high surface brightness (e.g., toward BN/KL and other outflows). Like the extended [C II] emission we have mapped, this FUV-exited H_2 emission traces the

Europe PMC Funders Author Manuscripts

Europe PMC Funders Author Manuscripts

FUV-illuminated face of Orion and may also dominate the extragalactic near-IR H_2 emission.

5.4. *An Explanation for the "[C II] Deficit"*

Figure 14 shows the spatial distribution of the two L[C II]/L_{FIR} regimes found toward OMC 1. Cyan contours for low ~10^{-4}–10^{-3} ratios toward the core of the cloud, and red contours for high ~10^{-3}–10^{-2} ratios toward the extended cloud face component (increasing from the center of OMC 1 and outwards). In Figure 14 (*left*), the L[C II]/L_{FIR} contours are shown on top of the $L_{\mathrm{FIR}}/M_{\mathrm{Gas}}$ map. Figure 14 (*right*) shows the same L[C II]/L_{FIR} contours on top of the $\tau_{\mathrm{d,160}}$ map.

5.4.1. *Geometry and N(C⁺) Relative to Total N*$_{\mathrm{H}}$ *Column*

—Since most of the [C II] emission arises from A_V<4 mag FUV-irradiated cloud surface layers, the local opacity of the dust grains mixed with the C^+ atoms ($\tau_{d,160}^{local}$) is generally small, $\tau_{d,160}^{local} \simeq N_H \cdot \mu\, m_{\mathrm{H}} \kappa_{160}/R_{gd} \approx 0.001$. Therefore, the dust opacity does not seem important locally, but it may be relevant if the [C II] sources are embedded in large columns of dust or if many [C II] emitting surfaces in a clumpy medium are included in the telescope beam.

The average 160 μm dust opacity inside the 200″ circle region surrounding the Trapezium is only moderate ($\tau_{\mathrm{d,160}} \simeq 0.06$ or A_V>50 mag). Therefore, the 160 μm continuum emission traces the column density of dust in the molecular cloud that lies behind the ionized nebula, weighted by T_{d}. The [C II] emission, however, does not arise from the entire line of sight but from the FUV-illuminated face of the cloud.

Figure 15 shows the L[C II]/L_{FIR} luminosity ratio as a function of $\tau_{\mathrm{d,160}}$. Both quantities are clearly tightly related. Therefore, the relative geometry of the illuminating stars with respect to the molecular cloud is important to understand the variations of L[C II]/L_{FIR}. Toward OMC 1, it can be idealized as a slab of constant [C II] emission arising from the *foreground* face of the molecular cloud (see a simplified sketch in Figure 16*a*). In this case, and for constant T_{d}, L[C II]/L_{FIR} would vary as $1/(1–e^{-\tau_{\mathrm{d,160}}})$, with $\tau_{\mathrm{d,160}}$ being proportional to the dust column toward each line of sight[15]. When this slab model is defined to intercept the median L[C II]/L_{FIR} and $\tau_{\mathrm{d,160}}$ values of the sample, the resulting curve satisfactorily reproduces the ~3 orders of magnitude L[C II]/L_{FIR} variations observed throughout the map (blue curve in Figure 15). The observed scatter with respect to the model is likely produced by small variations of T_{d}, grain charge, and of I[C II] in lines of sight with the same $\tau_{\mathrm{d,160}}$ but different G_0.

Gerin et al. (2015) have carried out small maps of the [C II] 158 μm line toward a limited sample[16] of more distant massive star-forming regions in the Milky Way (W31C, W49N, W51, DR21(OH), …). These observations show that the [C II] absorption produced by diffuse clouds on the line of sight can reduce the L[C II]/L_{FIR} ratio by ~50 %, if the v_{LSR} range of the absorbing clouds is not spectrally-resolved. Velocity-*unresolved* observations toward bright FIR continuum sources with foreground diffuse clouds thus result in apparently weaker [C II] luminosities. However, the most important effect revealed by the velocity-resolved [C II] emission observations is the decrease of L[C II]/L_{FIR} by large factors as one moves from the extended cloud component to the FIR continuum peak. Just like we have demonstrated in Orion (the L[C II]/L_{FIR} and the f=[N(C$^+$)/N_H]/1.4×10^{-4} maps shown in Figures 8(d) and 9(e) are similar), we believe that the decrease of L[C II]/L_{FIR} is due to the increase in the total column density throughout the cloud relative to the (surface) [C II] emitting column.

In addition, local low-metallicity galaxies such as the nearby LMC (e.g., Lebouteiller et al. 2012), but also early galaxies at z~6 (Capak et al. 2015), show enhanced [C II] emission relative to their FIR emission. These values are interpreted as the consequence of higher penetration of FUV photons due to the lower dust content (lower extinction). This agrees with our view of galaxies having clouds of larger C$^+$ column densities relative to their total dust column.

5.4.2. *Dust Attenuation*—The Trapezium cluster and associated H II region are only half enveloped by the molecular cloud. The [C II] emitting region is thus facing us and is mostly unattenuated by foreground dust. Other massive star-forming regions or galaxies may be *embedded* in large amounts of dust (buried star-bursts in galactic nuclei in particular). In such cases, the [C II] emission itself will be attenuated by $e^{-\tau_{d,160}}$ (a dust screen), where $\tau_{d,160}$ now represents the dust opacity between the observer and the [C II] emitting layers (Figure 16*c*). For $N(H_2) \gtrsim 10^{24}$ cm^{-2} ($\tau_{d,160} \gtrsim 1$), the expected L[C II]/L_{FIR} values can be very low, lower than 5×10^{-5} (black dotted curve in the inset of Figure 15). The prototypical example in the Milky Way is Sgr B2, the most massive starburst in the Galactic Center. Sgr B2 also shows a pronounced decrease of L[C II]/L_{FIR} as the dust opacity increases from the extended cloud to the (FIR) optically thick cores and embedded H II regions (e.g., Goicoechea et al. 2004; Etxaluze et al. 2013). This reasoning agrees with recent observations of local LIRGs in which the L[C II]/L_{FIR} deficit is restricted to their nuclei and not their extended disks (Díaz-Santos et al. 2014).

An intermediate case may exist in which the C$^+$ gas and the FIR emitting dust grains are well *mixed* through the entire line of sight (Figure 16*b*). In this case, the intrinsic [C II] emission will be attenuated by $(1 - e^{-\tau_{d,160}})/\tau_{d,160}$ (e.g., Thronson et al. 1990). This model provides less extreme corrections at large extinctions (magenta dashed curve in Figure 15). Given the surface origin of the [C II] emission, this model is however less realistic for OMC 1, but it may apply to low metallicity galaxies (lower A_V/N_H and dust-to-gas mass ratios) in which larger columns of C$^+$ relative to the total dust column exist due to the much higher penetration of the FUV radiation field.

Protostellar sources in Orion BN/KL are embedded in large column densities of material and thus very low L[C II]/L_{FIR} ratios can be expected. Using the *Herschel*/PACS spectroscopic data (Goicoechea et al. 2015) we derive L[C II]/$L_{FIR} \simeq 2.4 \times 10^{-5}$ and $\tau_{d,160} \simeq 2.7$ toward the hot core and IRc sources, and L[C II]/$L_{FIR} \simeq 7.7 \times 10^{-5}$ and $\tau_{d,160} \simeq 1.2$ toward the adjacent H_2 Peak 1 outflow region. Both positions are shown in the inset panel of Figure 15. In the frame of the simple geometrical models discussed above, the L[C II]/L_{FIR} ratio toward H_2 Peak 1 is still compatible with the *foreground* surface [C II] emission model. The L[C II]/L_{FIR} ratio toward the hot core is even lower, but this is likely a consequence of the higher FIR luminosity due to internal dust heating from the protostellar sources. In any case, the *embedded* [C II] emission model provides extinction corrections that are too large.

5.4.3. *Inhomogeneities and FUV radiation penetration*—The structure of molecular clouds is not perfectly homogeneous (e.g., Stutzki & Guesten 1990; Falgarone et al. 1991) and FUV radiation from massive stars can penetrate to deeper cloud depths than in homogeneous clouds. Our representative (homogeneous) PDR models for n_H=2×10$^{5-4}$ cm^{-3}, and dust grain properties appropriate to Orion, predict N(C$^+$)≃(1.2-1.6)×10^{18} cm^{-2}. These C$^+$ column densities are a factor of ≃2 larger than the predictions of PDR models using standard ISM grain properties (Section 3.2). However, they are still lower, by a factor of ~3, than the N(C$^+$) columns inferred toward many positions of OMC 1 (see Section 4). These higher values suggest a degree of inhomogeneity at ~ 25″ scales (~0.05 pc). As noted by Stacey et al. (1993), an inhomogeneous structure facilitates the propagation of FUV photons far from the Trapezium and contributes to the increase in the fraction of the volume that is effectively producing [C II] (more surfaces along the line of sight).

6. SUMMARY AND CONCLUSIONS

We have presented the first ~7.5′×11.5′ (~0.9 pc × 1.4 pc) velocity-resolved of map of the [C II] 158 μm line toward OMC 1. In combination with FIR photometry and H41α and CO J=2-1 line maps, we obtained the following results:

1. The main contribution to the [C II] luminosity (~85 %) is from the extended, FUV-illuminated face of the cloud (G_0>500, n_H>5×10^3 cm^{-3}) and from dense PDRs (G_0≳10^4, n_H≳10^5 cm^{-3}) at the interface between OMC 1 and the H II region surrounding the Trapezium cluster. In addition, ~15 % of the [C II] emission arises from a different gas component without CO counterpart. Part of this emission can be associated with filamentary structures that photoevaporate from the cloud and with depressions of the visible-light emission previously seen in the images of the Orion nebula (the Dark Bay, the Northern Dark Lane and other components in the atomic H I gas Veil). An additional but minor contribution can be associated with ionized gas.

2. The highest C$^+$ column density peaks are found toward the Trapezium, the Orion Bar, and specific PDRs to the east of BN/KL. These bright [C II] emission regions (T_P ≳ 150 K) follow a spherical shell structure (in projection on the sky) surrounding the back edge of the blister H II region. Several of these OMC 1/H II interfaces have nearly edge-on orientations. The excitation temperatures and line opacities derived from the [C II] and [^{13}C II] lines are T_{ex} = 250 – 300 K and $\tau_{[CII]}$ ≃ 1.5 – 3. Hence, the [C II] line toward these peaks is slightly optically thick, and traces high excitation dense PDR gas (T_k≳300 K and n_H≳10^5 cm^{-3}).

3. L[C II]/L_{FIR} decreases from the extended cloud component (~10^{-2}–10^{-3}) to the cloud center (~10^{-3}–10^{-4}). The latter values are reminiscent of the "[C II] line deficit" seen toward local ULIRGs. The L[C II]/L_{FIR} variations can be explained by the approximately face-on geometry of the molecular cloud relative to the externally illuminating stars. This creates a [C II] emission layer at the FUV-

illuminated surface of the cloud. The FIR emission, however, approximately traces the bulk of material along each line of sight. Indeed, L[C II]/L_{FIR} is spatially correlated with the dust column density in a way that agrees with a simple face-on slab model. Trying to link the local and the extragalactic emission, we conclude that the [C II] emitting column relative to the total dust column density along each line of sight determines the observed L[C II]/L_{FIR} variations, with the lowest ratios observed toward the highest column density peaks. This also implies that the specific grain properties and dust-to-gas mass ratio are important parameters in determining the L[C II]/L_{FIR} ratio.

4. We show that the L_{FIR}/M_{Gas} ratio follows the hydrogen ionizing photons traced by the H41α line, reaching $L_{FIR}/M_{Gas}>80L_{\odot}M_{\odot}^{-1}$ toward the H II region around the Trapezium. These high L_{FIR}/M_{Gas} values are interesting proxies of the ionization parameter U, and are similar to the threshold where luminous galaxy mergers start to show "[C II] emission deficits". Indeed, the surface densities we infer toward OMC 1 ($\Sigma_{Gas}\simeq2000$ $M_{\odot}$ pc^{-2} and Σ_{SFR}=(2.3-3.4)×10^{-5} $M_{\odot}$ yr^{-1} pc^{-2}) are comparable to those inferred in galaxies hosting vigorous star-formation. The interesting point of course is that these conditions, those of a young massive cluster still surrounded by its dense parental molecular cloud, can dominate the FIR emission at kpc galactic scales.

The [C II] 158 μm line is undoubtedly a bright and powerful diagnostic of the FUV-illuminated ISM. In combination with other tracers ([O I], CO, dust SEDs, PAHs and H I), a very detailed picture of the dominant environment and prevailing physical conditions can be extracted. In addition, observations of molecular ions (CO^+, HOC^+, CF^+ or CH^+) directly related to C^+, are becoming interesting tools to constrain the properties of the "C^+ layers" in FUV-illuminated H_2 gas (e.g., Störzer et al. 1995; Fuente et al. 2003; Neufeld 2006; Guzmán et al. 2012; Nagy et al. 2013). Even more *exotic* ions such as OH^+ or ArH^+ are more specific tracers of low H_2 fraction (nearly atomic) gas where [C II] is also expected (Neufeld et al. 2010; van der Tak et al. 2013; Schilke 2014). Most of them can be observed with ALMA.

Acknowledgments

We acknowledge helpful comments and suggestions from our referee. We thank Spanish MINECO for funding support under grants CSD2009-00038, AYA2009-07304 and AYA2012-32032. We also thank the ERC for support under grant ERC-2013-Syg-610256-NANOCOSMOS. Part of this research was carried out at the Jet Propulsion Laboratory (JPL), California Institute of Technology (Caltech), under a contract with the National Aeronautics and Space Administration (NASA). Support for this work was provided by NASA through an award issued by JPL/Caltech. This work was supported by the German *Deutsche Forschungsgemeinschaft, DFG* project number SFB 956, C1. This work was in part supported by the CNRS program "Physique et Chimie du Milieu Interstellaire (PCMI)".

Facilities: Herschel Space Observatory, IRAM-30m

Notes Added after Proofs: Three relevant papers were discovered after proof reading, below we include their most pertinent information related to this work:

- O'Dell & Harris (2010, AJ, 140, 985) presented a more detailed geometrical model of the Orion molecular cloud, Orion nebula and Veil (see their Figure 13).
- Díaz-Santos et al. (2013, ApJ, 774, 68) determined the L[C II]/L_{FIR} ratio in a sample of 202 local LIRG and ULIRG galaxies. The L[C II]/L_{FIR} ratio was found to scale with the strength of the the 9.7 μm

silicate absorption feature, except for "optically thick" galaxies showing very large 9.7 μm strengths. Unlike the MIR dust emission/absorption, the FIR/submm emission is more sensitive to the total column density of dust in dense clouds. Thus, their observed trend is consistent with our detailed interpretation of the L[C II]/L_{FIR} variations.

- Compared to local ULIRGs, Rigopoulou et al. (2014, ApJL, 781, L15) found enhanced L[C II]/L_{FIR} luminosity ratios in a sample of *intermediate* redshift (0.2<z<0.8) ULIRGs observed with *Herschel*/SPIRE. This result is more similar to observations of *high* red-shift galaxies with ALMA, and can also be understood as variations of the [C II] emitting column relative to the total dust column density toward each galaxy.

APPENDIX: SED FITTING EXAMPLES

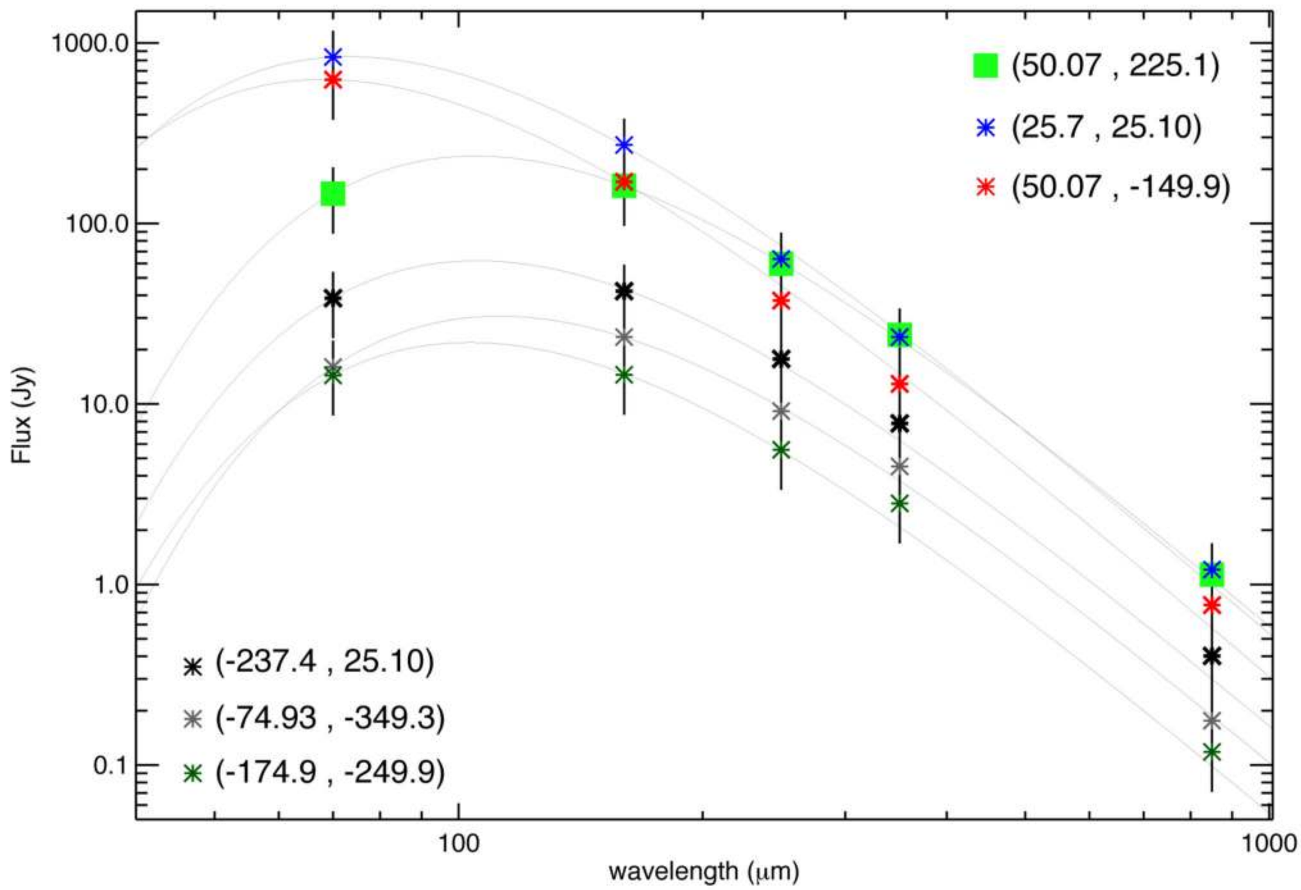

Figure 17.

Appendix: Example of SED fits to *Herschel*/PACS-SPIRE and *JCMT*/SCUBA2 photometric data in Jy/pixel units. All convolved at a uniform angular resolution of 25″. Selected positions are indicated by their offsets with respect to the map center in arcsec.

REFERENCES

Abel NP. MNRAS. 2006; 368:1949.

Abel NP, Ferland GJ, O'Dell CR, Shaw G, Troland TH. ApJ. 2006b; 644:344.

Abel NP, Dudley C, Fischer J, Satyapal S, van Hoof PAM. ApJ. 2009; 701:1147.

Allamandola LJ, Tielens AGGM, Barker JR. ApJS. 1989; 71:733.

Europe PMC Funders Author Manuscripts

Allers KN, Ja e DT, Lacy JH, Draine BT, Richter MJ. ApJ. 2005; 630:368.

André P, Men'shchikov A, Bontemps S, et al. A&A. 2010; 518:LL102.

Audit E, Hennebelle P. A&A. 2005; 433:1.

Arab H, Abergel A, Habart E, et al. A&A. 2012; 541:A19.

Baldwin JA, Ferland GJ, Martin PG, et al. ApJ. 1991; 374:580.

Bally J, Langer WD, Stark AA, Wilson RW. ApJ. 1987; 312:L45.

Bally J. hsf1. 2008; 459

Barinovs Ğ, van Hemert MC, Krems R, Dalgarno A. ApJ. 2005; 620:537.

Bernard-Salas J, Habart E, Arab H, et al. A&A. 2012; 538:AA37.

Berné O, Marcelino N, Cernicharo J. ApJ. 2014; 795:13.

Bertoldi F, Draine BT. ApJ. 1996; 458:222.

Blake GA, Sutton EC, Masson CR, Phillips TG. ApJ. 1987; 315:621.

Boreiko RT, Betz AL. ApJ. 1996; 467:L113.

Brisbin D, Ferkinho C, Nikola T, et al. ApJ. 2015; 799:13.

Brogan CL, Troland TH, Abel NP, Goss WM, Crutcher RM. ASPC. 2005; 343:183.

Brown JM, Evenson KM, Zink LR. Phys. Rev. A. 1993; 48:3761. [PubMed: 9910047]

Capak PL, Carilli C, Jones G, et al. Nature. 2015; 522:455. [PubMed: 26108853]

Cardelli JA, Clayton GC, Mathis JS. ApJ. 1989; 345:245.

Carilli CL, Walter F. ARA&A. 2013; 51:105.

Chen J-H, Goldsmith PF, Viti S, et al. ApJ. 2014; 793:111.

Cooksy AL, Blake GA, Saykally RJ. ApJ. 1986; 305:L89.

Crawford MK, Genzel R, Townes CH, Watson DM. ApJ. 1985; 291:755.

Cuadrado S, Goicoechea JR, Pilleri P, et al. A&A. 2015; 575:A82.

Cubick M, Stutzki J, Ossenkopf V, Kramer C, Rollig M. A&A. 2008; 488:623.

Dalgarno A, McCray RA. ARA&A. 1972; 10:375.

de Graauw T, Helmich FP, Phillips TG, et al. A&A. 2010; 518:LL6.

Díaz-Santos T, Armus L, Charmandaris V, et al. ApJ. 2014; 788:LL17.

Draine BT. ApJ. 2011; 732:100.

Etxaluze M, Goicoechea JR, Cernicharo J, et al. A&A. 2013; 556:AA137.

Falgarone E, Phillips TG, Walker CK. ApJ. 1991; 378:186.

Fuente A, Rodrıguez-Franco A, Garcıa-Burillo S, Martın-Pintado J, Black JH. A&A. 2003; 406:899.

Gao Y, Solomon PM. ApJ. 2004; 606:271.

Genzel R, Stutzki J. ARA&A. 1989; 27:41.

Genzel R, Tacconi LJ, Gracia-Carpio J, et al. MNRAS. 2010; 407:2091.

Gerin M, Ruaud M, Goicoechea JR, et al. A&A. 2015; 573:AA30.

Goicoechea JR, Rodríguez-Fernández NJ, Cernicharo J. ApJ. 2004; 600:214.

Goicoechea JR, Pety J, Gerin M, et al. A&A. 2006; 456:565.

Goicoechea JR, Le Bourlot J. A&A. 2007; 467:1.

Goicoechea JR, Chavarría L, Cernicharo J, et al. ApJ. 2015; 799:102.

Goldsmith PF, Bergin EA, Lis DC. ApJ. 1997; 491:615.

Goldsmith PF, Langer WD, Pineda JL, Velusamy T. ApJS. 2012; 203:13.

González-Alfonso E, Fischer J, Sturm E, et al. ApJ. 2015; 800:69.

Graciá-Carpio J, Sturm E, Hailey-Dunsheath S, et al. ApJ. 2011; 728:LL7.

Graf UU, Simon R, Stutzki J, et al. A&A. 2012; 542:L16.

Grenier IA, Casandjian J-M, Terrier R. Sci. 2005; 307:1292.

Griffin MJ, Abergel A, Abreu A, et al. A&A. 2010; 518:L3.

Guzmán V, Pety J, Gratier P, et al. A&A. 2012; 543:LL1.

Habing HJ. Bull. Astron. Inst. Netherlands. 1968; 19:421.

Herrera-Camus R, Bolatto AD, Wolfire MG, et al. ApJ. 2015; 800:1.

Herrmann F, Madden SC, Nikola T, et al. ApJ. 1997; 481:343.
Hildebrand RH. QJRAS. 1983; 24:267.
Hogerheijde MR, Jansen DJ, van Dishoeck EF. A&A. 1995; 294:792.
Holland WS, Bintley D, Chapin EL, et al. MNRAS. 2013; 430:2513.
Hollenbach DJ, Tielens AGGM. RvMP. 1999; 71:173.
Ingalls JG, Reach WT, Bania TM. ApJ. 2002; 579:289.
Kapala MJ, Sandstrom K, Groves B, et al. ApJ. 2015; 798:24.
Kaufman MJ, Wolfire MG, Hollenbach DJ, Luhman ML. ApJ. 1999; 527:795.
Kennicutt RC Jr. ApJ. 1998; 498:541.
Kester D, Avruch I, Teyssier D. AIPC. 2014; 1636:62.
Lada CJ, Lombardi M, Alves JF. ApJ. 2010; 724:687.
Lada CJ, Forbrich J, Lombardi M, Alves JF. ApJ. 2012; 745:190.
Langer WD, Penzias AA. ApJ. 1990; 357:477.
Lebouteiller V, Cormier D, Madden SC, et al. A&A. 2012; 548:A91.
Le Petit F, Nehmé C, Le Bourlot J, Roueff E. ApJS. 2006; 164:506.
Lee TA. ApJ. 1968; 152:913.
Li A, Draine BT. ApJ. 2001; 554:778.
Lilley AE, Palmer P. ApJS. 1968; 16:143.
Lis DC, Serabyn E, Keene J, et al. ApJ. 1998; 509:299.
Luhman ML, Ja e DT, Keller LD, Pak S. ApJ. 1994; 436:L185.
Luhman ML, Satyapal S, Fischer J, et al. ApJ. 1998; 504:L11.
Madden SC, Geis N, Genzel R, et al. ApJ. 1993; 407:579.
Madden SC, Poglitsch A, Geis N, Stacey GJ, Townes CH. ApJ. 1997; 483:200.
Malhotra S, Helou G, Stacey G, et al. ApJ. 1997; 491:L27.
Malhotra S, Kaufman MJ, Hollenbach D, et al. ApJ. 2001; 561:766.
Megeath ST, Gutermuth R, Muzerolle J, et al. AJ. 2012; 144:192.
Mookerjea B, Ghosh SK, Kaneda H, et al. A&A. 2003; 404:569.
Nagy Z, Van der Tak FFS, Ossenkopf V, et al. A&A. 2013; 550:AA96.
Nakagawa T, Yui YY, Doi Y, et al. ApJS. 1998; 115:259.
Neufeld DA, Schilke P, Menten KM, et al. A&A. 2006; 454:L37.
Neufeld DA, Goicoechea JR, Sonnentrucker P, et al. A&A. 2010; 521:LL10.
Ochsendorf BB, Tielens AGGM. A&A. 2015; 576:A2.
O'Dell CR. ARA&A. 2001; 39:99.
O'Dell CR, Yusef-Zadeh F. AJ. 2000; 120:382.
O'Dell CR, Henney WJ, Abel NP, Ferland GJ, Arthur SJ. AJ. 2009; 137:367.
Okada Y, Pilleri P, Berné O, et al. A&A. 2013; 553:A2.
Ossenkopf V, Röllig M, Neufeld DA, et al. A&A. 2013; 550:AA57.
Phillips TG, Huggins PJ, Wannier PG, Scoville NZ. ApJ. 1979; 231:720.
Pilbratt GL, Riedinger JR, Passvogel T, et al. A&A. 2010; 518:LL1.
Pineda JL, Langer WD, Velusamy T, Goldsmith PF. A&A. 2013; 554:AA103.
Pineda JL, Langer WD, Goldsmith PF. A&A. 2014; 570:AA121.
Plume R, Kaufman MJ, Neufeld DA, et al. ApJ. 2004; 605:247.
Poglitsch A, Waelkens C, Geis N, et al. A&A. 2010; 518:L2.
Riechers DA, Carilli CL, Capak PL, et al. ApJ. 2014; 796:84.
Rivilla VM, Martín-Pintado J, Jiménez-Serra I, Rodríguez-Franco A. A&A. 2013; 554:AA48.
Robberto M, Soderblom DR, Bergeron E, et al. ApJS. 2013; 207:10.
Roelfsema PR, Helmich FP, Teyssier D, et al. A&A. 2012; 537:AA17.
Rodriguez-Fernandez NJ, Braine J, Brouillet N, Combes F. A&A. 2006; 453:77.
Rodriguez-Franco A, Martin-Pintado J, Fuente A. A&A. 1998; 329:1097.

Europe PMC Funders Author Manuscripts

Rosenthal D, Bertoldi F, Drapatz S. A&A. 2000; 356:705.

Russell RW, Melnick G, Gull GE, Harwit M. ApJ. 1980; 240:L99.

Sanders DB, Mirabel IF. ARA&A. 1996; 34:749.

Schilke P, Neufeld DA, Müller HSP, et al. A&A. 2014; 566:AA29.

Simón-Díaz S, Herrero A, Esteban C, Najarro F. A&A. 2006; 448:351.

Simón-Díaz S, Stasińska G. A&A. 2011; 526:AA48.

Sofia UJ, Lauroesch JT, Meyer DM, Cartledge SIB. ApJ. 2004; 605:272.

Stacey GJ, Geis N, Genzel R, et al. ApJ. 1991; 373:423.

Stacey GJ, Townes CH, Geis N, et al. ApJ. 1991b; 382:L37.

Stacey GJ, Ja e DT, Geis N, et al. ApJ. 1993; 404:219.

Stacey GJ, Hailey-Dunsheath S, Ferkinhoff C, et al. ApJ. 2010; 724:957.

Störzer H, Stutzki J, Sternberg A. A&A. 1995; 296:L9.

Störzer H, Hollenbach D. ApJ. 1998; 495:853.

Stutzki J, Guesten R. ApJ. 1990; 356:513.

Tercero B, Cernicharo J, Pardo JR, Goicoechea JR. A&A. 2010; 517:AA96.

Thronson HA Jr. Majewski S, Descartes L, Hereld M. ApJ. 1990; 364:456.

Tielens AGGM, Hollenbach D. ApJ. 1985; 291:722.

Tielens AGGM, Hollenbach D. ApJ. 1985b; 291:747.

Troland TH, Heiles C, Goss WM. ApJ. 1989; 337:342.

van der Tak FFS, Nagy Z, Ossenkopf V, et al. A&A. 2013; 560:AA95.

van der Werf PP, Goss WM, O'Dell CR. ApJ. 2013; 762:101.

Wiesenfeld L, Goldsmith PF. ApJ. 2014; 780:183.

Wilson NJ, Bell KL. MNRAS. 2002; 337:1027.

Wolfire MG, Hollenbach D, McKee CF. ApJ. 2010; 716:1191.

Wu J, Evans NJ II, Gao Y, et al. ApJ. 2005; 635:L173.

Wyrowski F, Schilke P, Hofner P, Walmsley CM. ApJ. 1997; 487:L171.

Zuckerman B. ApJ. 1973; 183:863.

Europe PMC Funders Author Manuscripts

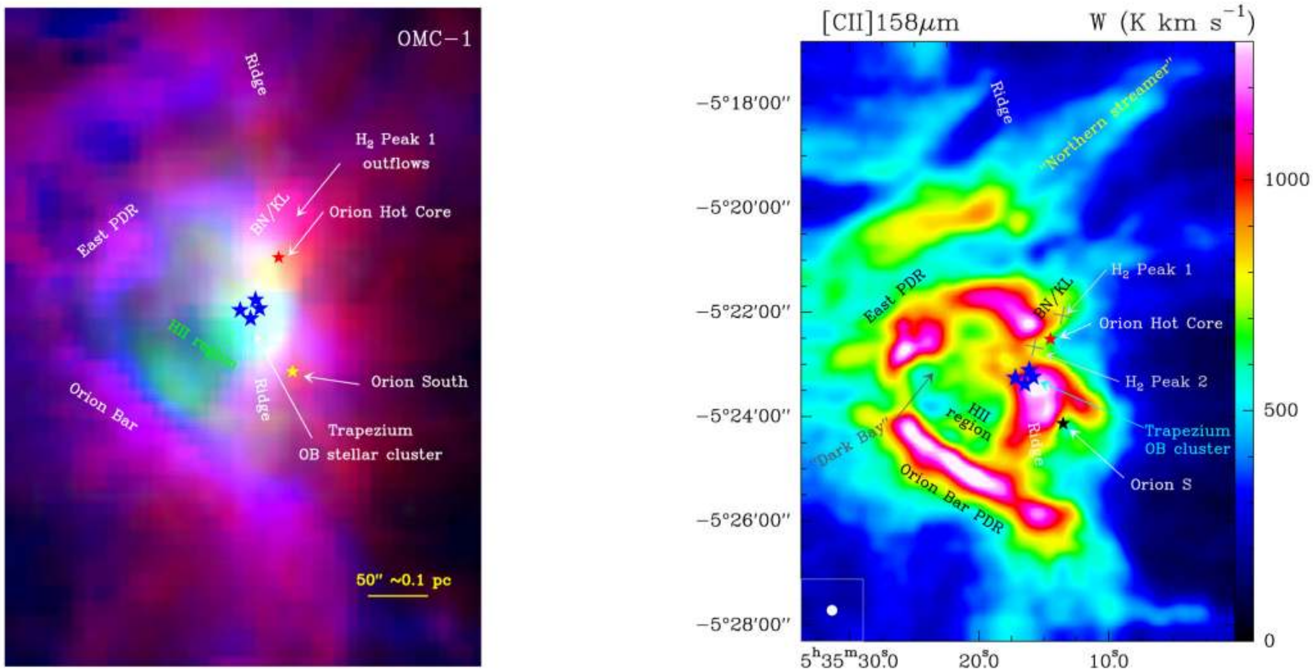

Figure 1.

(Left): Composite image with the H41α (green), [C II] 158 μm (blue) and CO 2-1 (red) integrated line intensities. The positions of the main sources in OMC 1 are shown. (Right): *Herschel*/HIFI map of the total [C II] 158 μm integrated line intensity[3] (in K km s^{-1}) from v_{LSR}=−30 to +30 km s^{-1}.

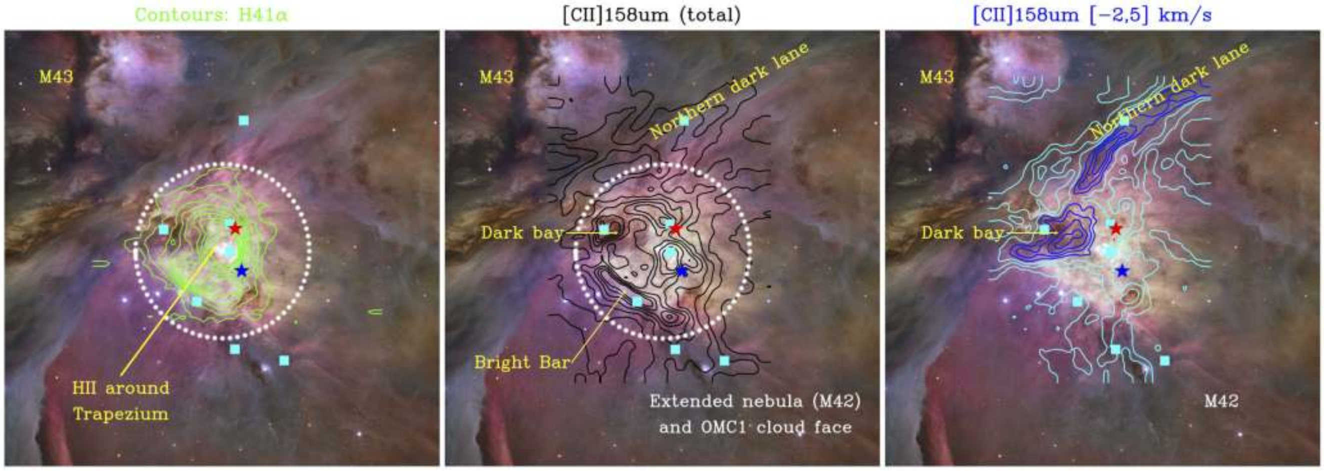

Figure 2.

Color-composite visible image of the Orion Nebula (M42) taken with the ACS instrument on board the *Hubble Space Telescope (HST)*. The assigned colors are: red and orange for [S II] and Hα, blue for *B*, and green for *V* filters respectively (Robberto et al. 2013). *(Left)*: Green contours show the integrated intensity (*W*) of the H41α recombination line (from 3 to 21 K km s^{-1} in steps of 2 K km s^{-1}). The white dotted 200″ (0.4 pc) radius circle is centered on θ^1 Ori C, the brightest star of the Trapezium. We define the "extended cloud face" component to lie outside this circle. *Middle*: Black contours show the total [C II] 158 μm integrated intensity (v$_{LSR}$=−30 to +30 km s^{-1} with *W* from 0 to 1300 K km s^{-1} in steps of 150 K km s^{-1}). *Right*: [C II] "blue-shifted streamer" (emission from v$_{LSR}$=−2 to +5 km $^{-1}$) with *W* from 0 to 60 K km s^{1} (cyan) and from 80 to 140 K km s^{1} (blue), all in steps of 20 K km s^{-1}. This emission coincides with the *Northern dark lane* and with the *Dark bay* seen in visible-light images of the Nebula. The Orion hot core in the BN/KL region and Orion S positions are indicated by red and blue stars respectively. The positions where line spectra have been extracted (shown in Figure 3) are indicated by cyan squares.

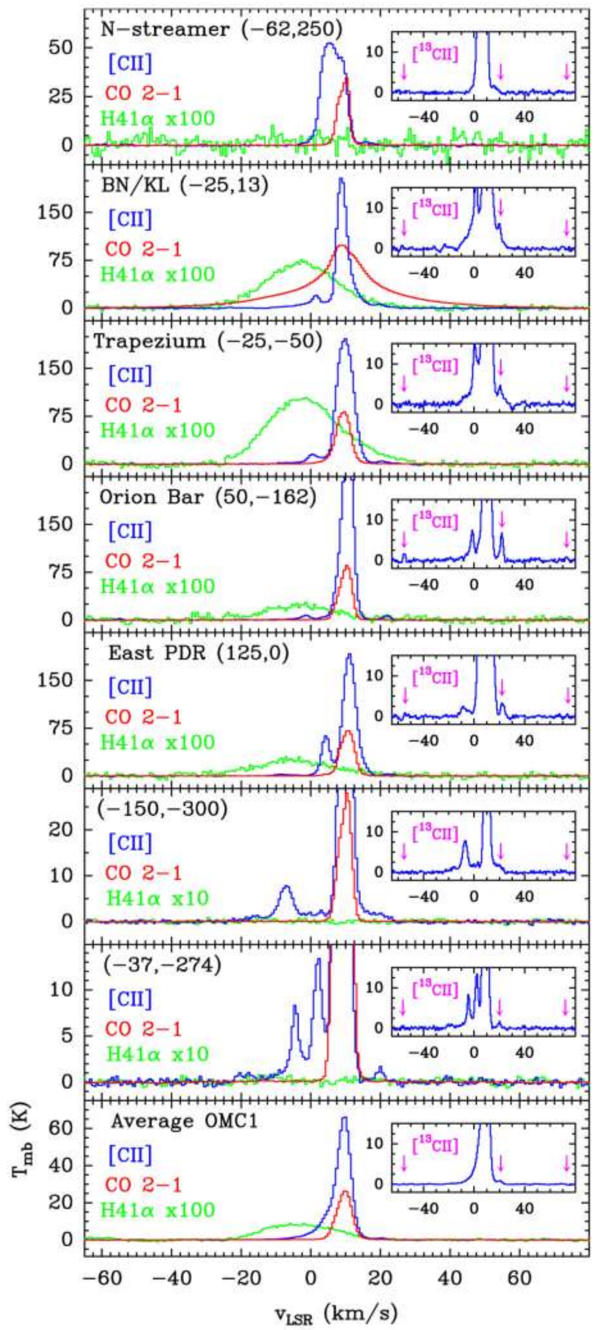

Figure 3.

[C II] 158 μm, CO 2-1 and H41α line profiles toward representative positions in Orion. Offsets in arcsec are given with respect to the HIFI map center at α_{2000}: $5^h35^m17.0^s$, δ_{2000}: $-5°22'33.7''$. The last panel shows the average spectrum over the region. The inset panels show a zoom into the spectra. The magenta arrows mark the expected positions of the [^{13}C II] F=1-0, 2-1 and 1-1 hyperfine components (from left to right). The [C II] and CO spectra were extracted from maps convolved to 25″ resolution.

Europe PMC Funders Author Manuscripts

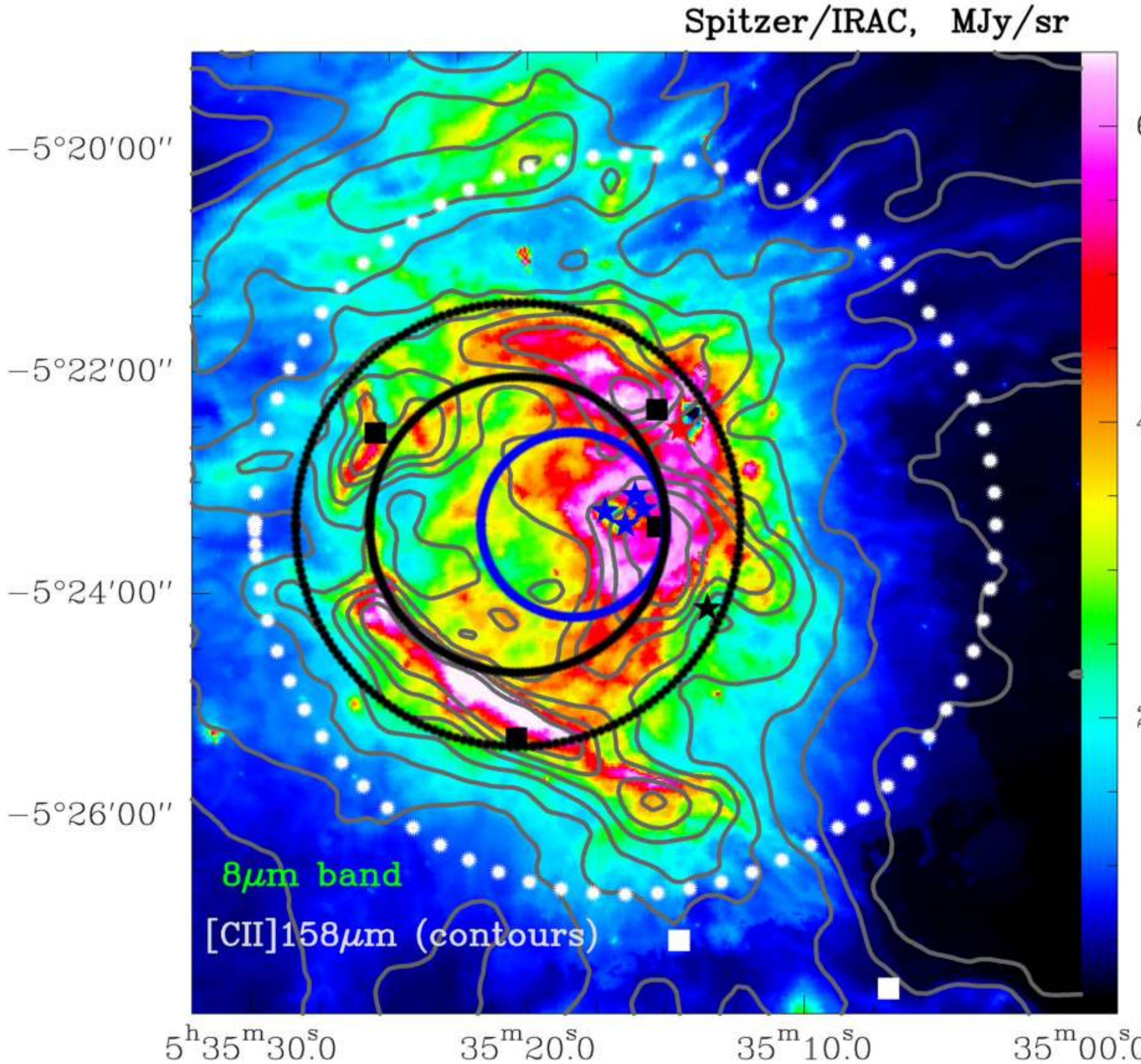

Figure 4.

Spitzer/IRAC 8 μm filter image (dominated by PAH emission) toward OMC 1. Contours show the total [C II] 158 μm integrated intensity (from 0 to 1300 K km s^{-1} in steps of 150 K km s^{-1}). The different circles and regions are defined in Section 3.2. The positions where line spectra have been extracted (shown in Figure 3) are indicated by squares.

Europe PMC Funders Author Manuscripts

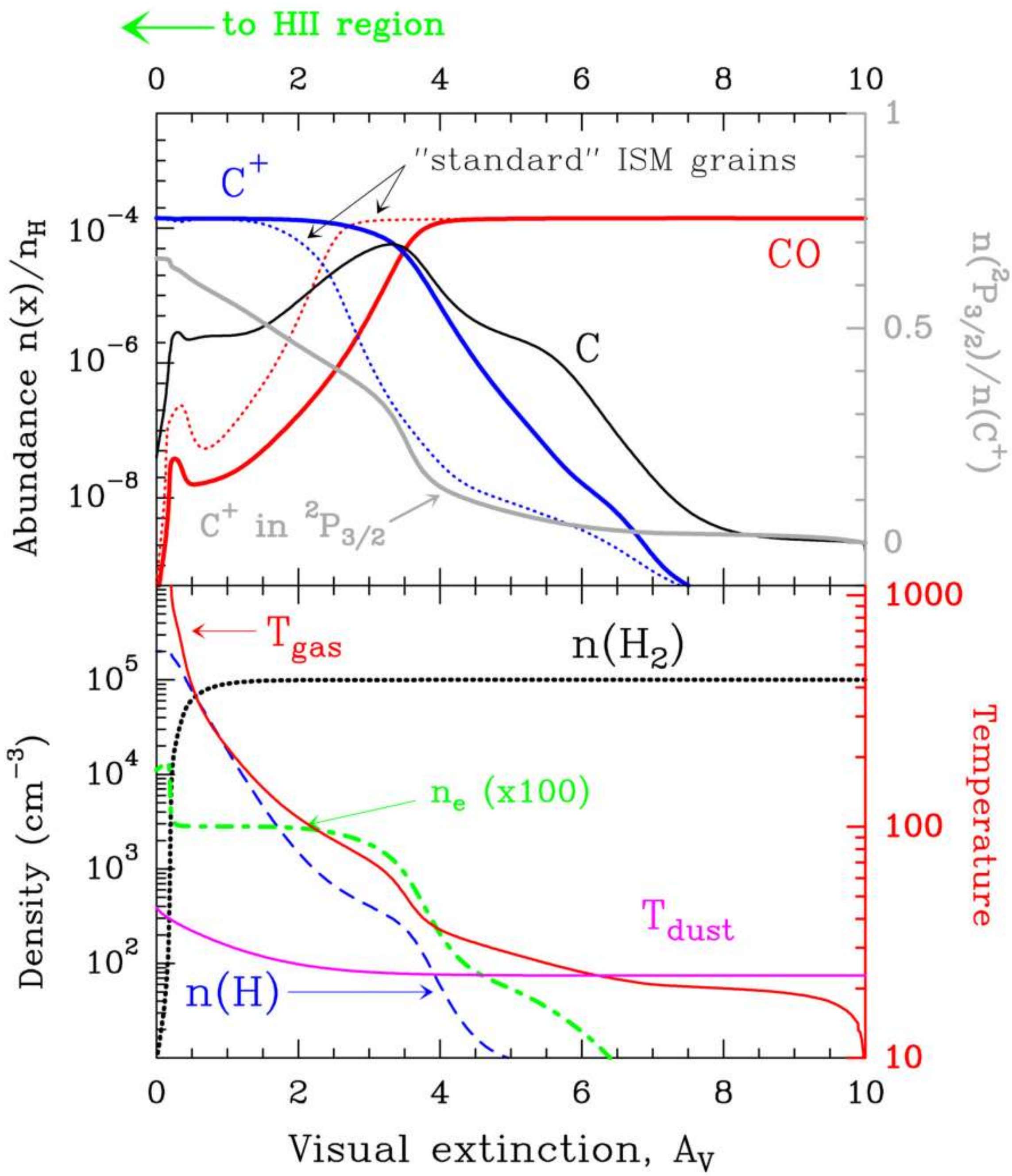

Figure 5.

H/H_2 and C^+/C/CO transitions predicted by the *Meudon* PDR code for physical conditions and grain properties representative of OMC 1 near the Trapezium cluster (G_0=2×10^4 and n_H=n(H)+2 $n(H_2)$=2×10^5 cm^{-3}). The equivalent length of the A_V=10 mag slab is ≃10,000 AU (≃24″ at the distance to OMC 1). The dotted C^+ and CO abundance profiles in the upper panel are obtained using standard, diffuse ISM, grain properties (see Section 3.2).

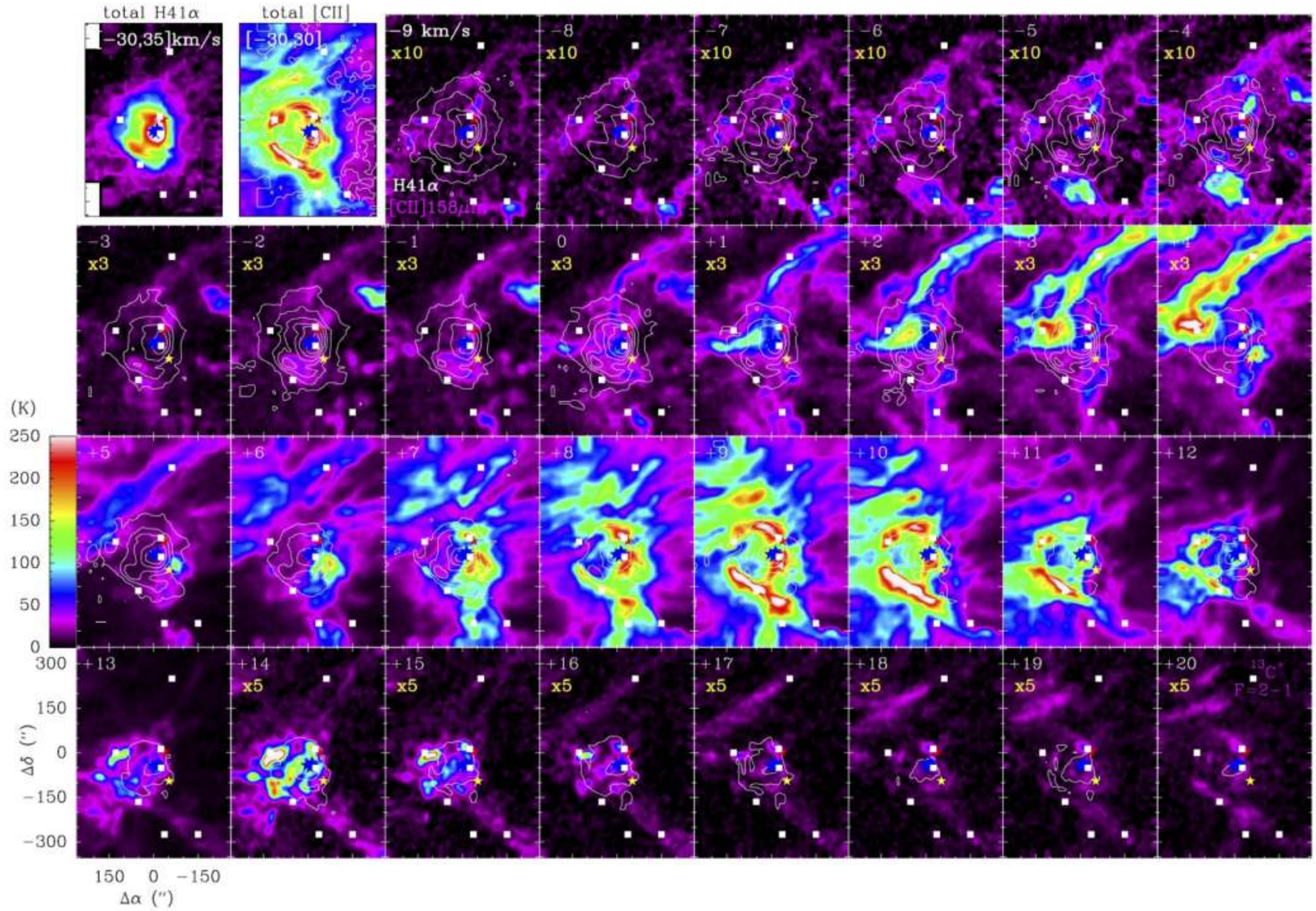

Figure 6.

Velocity channel maps in steps of 1 km s^{-1} from v_{LSR} = −9 to +20 km s^{-1} ([C II] in colors and H41α line in contours). The [C II] main beam temperature scale in bins of 1 km s^{-1} is given in the color wedge (in some velocity intervals the [C II] intensity per channel is multiplied by a factor that is specified in each panel). Offsets in arcsec are given with respect to the HIFI map center. The H41α contours go from 0.2 to 1.8 K km s^{-1} in steps of 0.3 K km s^{-1}. The [C II] emission seen at v_{LSR} = +20 km s^{-1} (last panel) is dominated by the [^{13}C II] F=2-1 line peak. Note that the first two upper-left panels show total integrated line intensity maps for H41α (from 0 to 22 K km s^{-1}) and [C II] 158 μm (from 0 to 1300 K km s^{-1}). In the total [C II] intensity map, H41α integrated line intensities are shown as white contours (from 1 to 21 K km s^{-1} in steps of 4 K km s^{-1}). The Orion hot core, Orion S condensation and Trapezium stars are indicated by red, yellow and blue stars respectively. The positions where line spectra have been extracted (shown in Figure 3) are indicated by white squares.

Europe PMC Funders Author Manuscripts

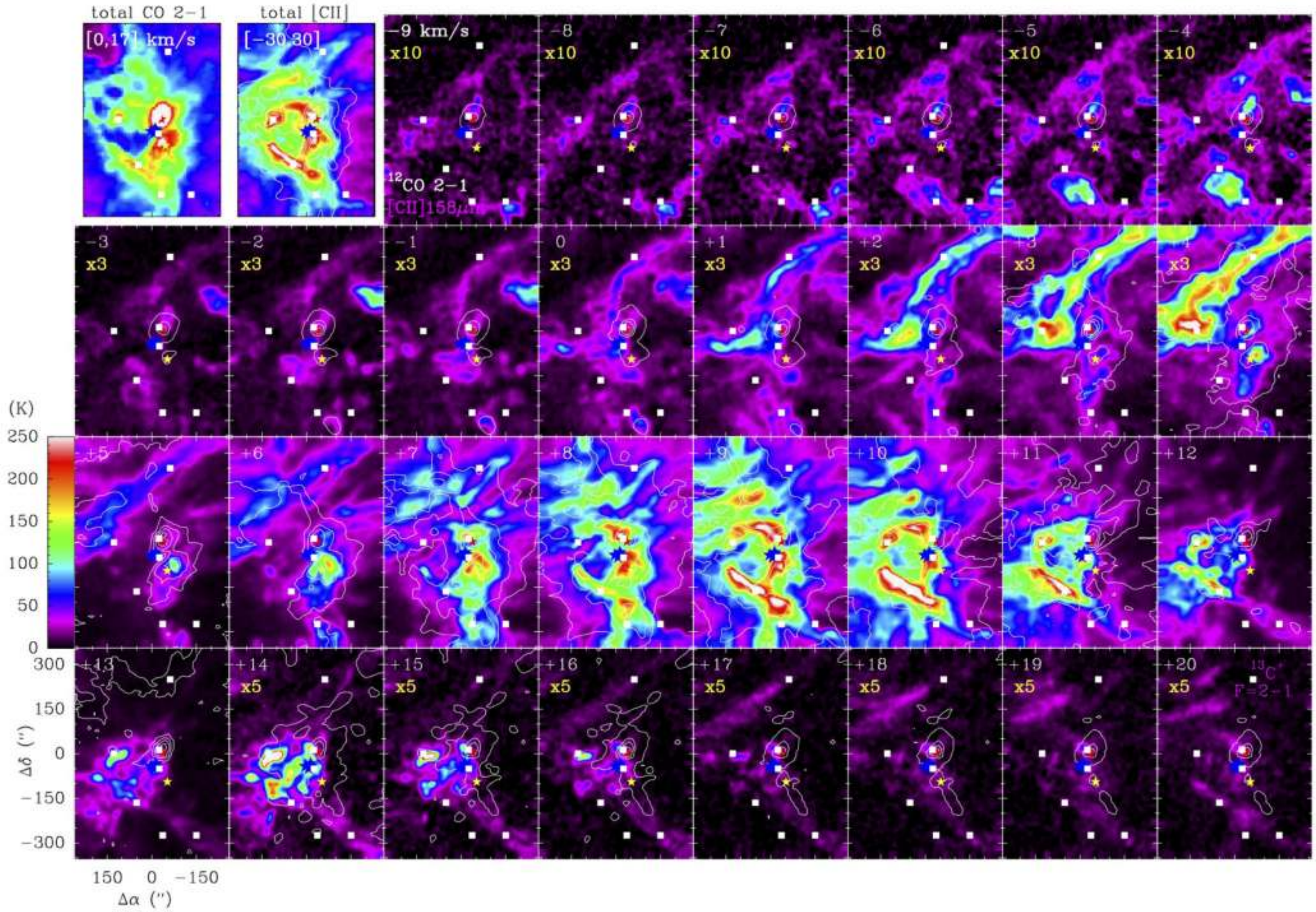

Figure 7.

Same as Figure 6 but the CO 2-1 line (in contours). The CO 2-1 contours go from 1.5 to 160 K km s^{-1} in steps of 30 K km s^{-1}. The high velocity CO 2-1 emission (v_{LSR}<0 s^{-1} and v_{LSR}>15 s^{-1}) mostly arises from molecular outflows around Orion BN/KL and Orion S protostellar sources. At other positions, the observed [C II] emission in these velocity ranges does not have CO emission counterpart (e.g., the blue-shifted [C II] streamer at v_{LSR}=−2 to +5 km $^{-1}$, or the [C II] emission in the southwest at $v_{LSR} \gtrsim$ 12 km s^{-1} beyond the Orion Bar). The first two upper-left panels show total integrated line intensity maps of CO 2-1 (from 0 to 600 K km s^{-1}) and [C II] 158 μm (from 0 to 1300 K km s^{-1}). In the [C II] total intensity map, CO 2-1 integrated line intensities are shown as white contours, from 200 to 500 K km s^{-1} in steps of 100 K km s^{-1} (extended emission) and from 800 to 1400 K km s^{-1} in steps of 200 K km s^{-1} (Orion BN/KL outflows).

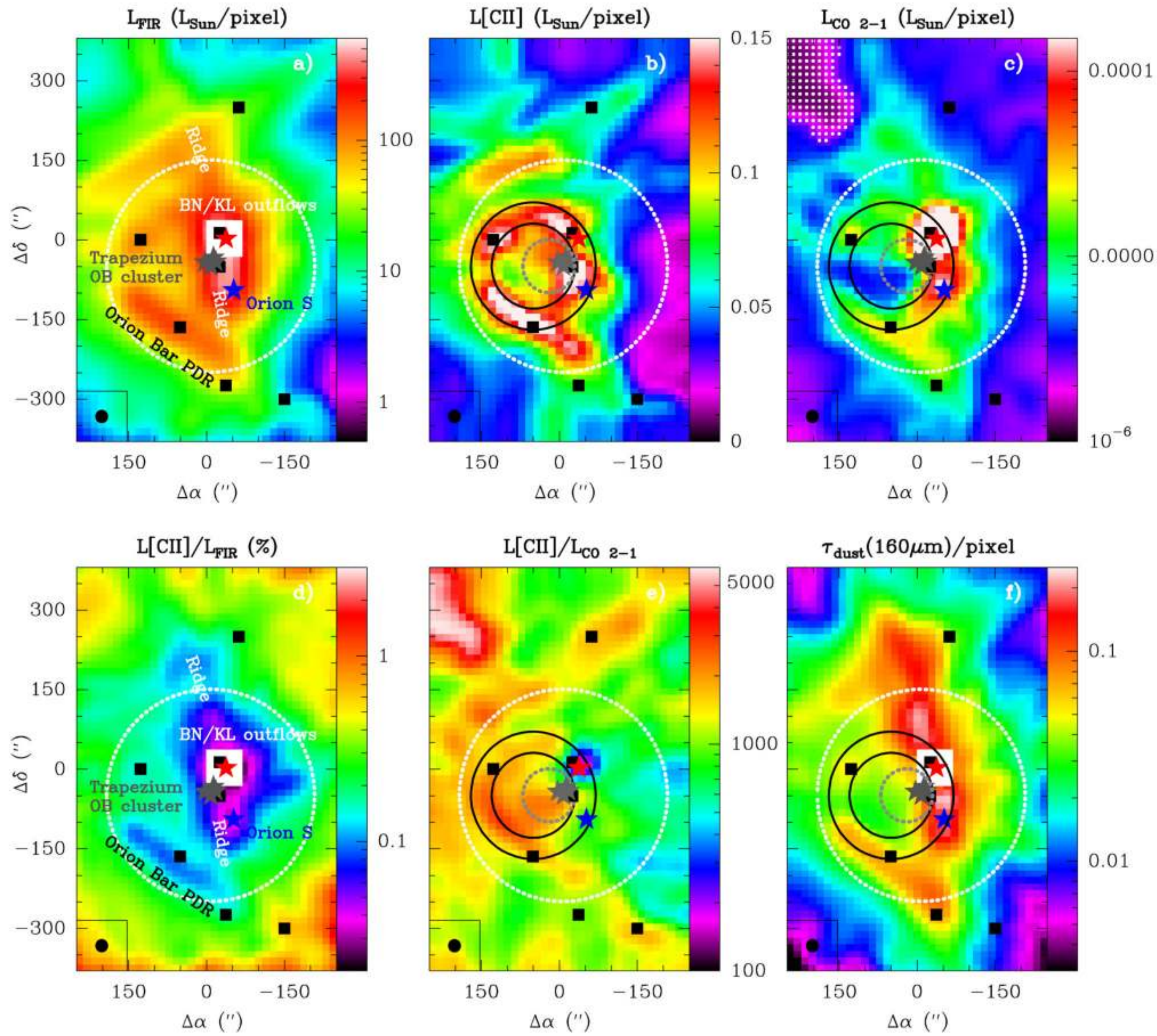

Figure 8.

Luminosity and dust opacity per pixel maps toward OMC1 convolved to 25″ resolution. (a) $L_{\rm FIR}$ map ($G_0 \simeq 200\ L_{\rm FIR}/L_\odot$ per pixel, see footnote 11), (b) L[C II], (c) $L_{\rm CO\ 2-1}$ (from Berné et al. 2014), (d) L[C II]/$L_{\rm FIR}$ in %, (e) L[C II]/$L_{\rm CO\ 2-1}$, and (f) dust opacity at 160 μm from SED fits. The white squares in panel (c) represent positions of low $L_{\rm CO\ 2-1}$ and high L[C II]/$L_{\rm CO\ 2-1}$ ratios (up to ~5000) in panel (e) see also Figure 11f. The different circles and regions are defined in Section 3.2. The black squares indicate the positions of the spectra shown in Figure 3. The white square areas in the central BN/KL region indicate positions where the *Herschel* photometric observations are saturated.

Europe PMC Funders Author Manuscripts

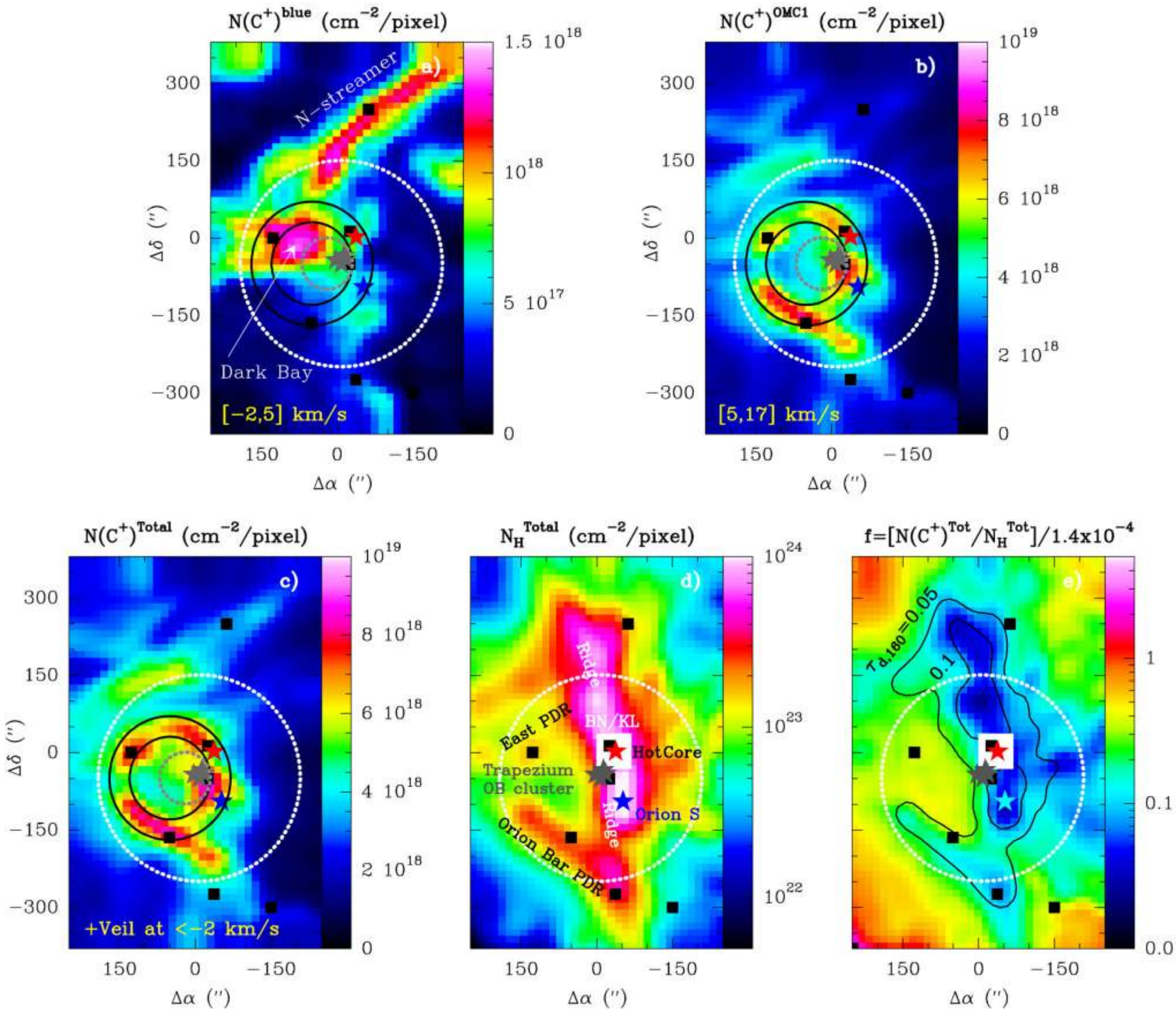

Figure 9.

Column density per pixel maps toward Orion. (a) $N(C^+)^{blue}$ extracted from the blue-shifted emission component from v_{LSR}=−2 to +5 km $^{-1}$. (b) $N(C^+)^{OMC1}$ extracted from the main emission component from v_{LSR}=+5 to +17 km $^{-1}$. (c) $N\left(C^+\right)^{Total}=N\left(C^+\right)^{OCM1}+N\left(C^+\right)^{blue}+N\left(C^+\right)^{<-2\ km/s}$, where $N(C^+)^{<-2\ km/s}=10^{17}$ cm^{-2} is adopted in all positions (see text). (d) $N_H^{Total}=N(H)+2N(H_2)$ from the dust emission. (e) $\left[N\left(C^+\right)^{Total}/N_H^{Total}\right]/1.4\times10^{-4}$ color map, this is roughly the fraction (*f*) of the total column density traced by [C II] toward Orion. This fraction scales with the total column density of dust along each line of sight. The 160 μm dust opacity iso-contours at $\tau_{d,160}$=0.1 (inner) and 0.05 (outer) are shown in black. The different circles are defined in Section 3.2.

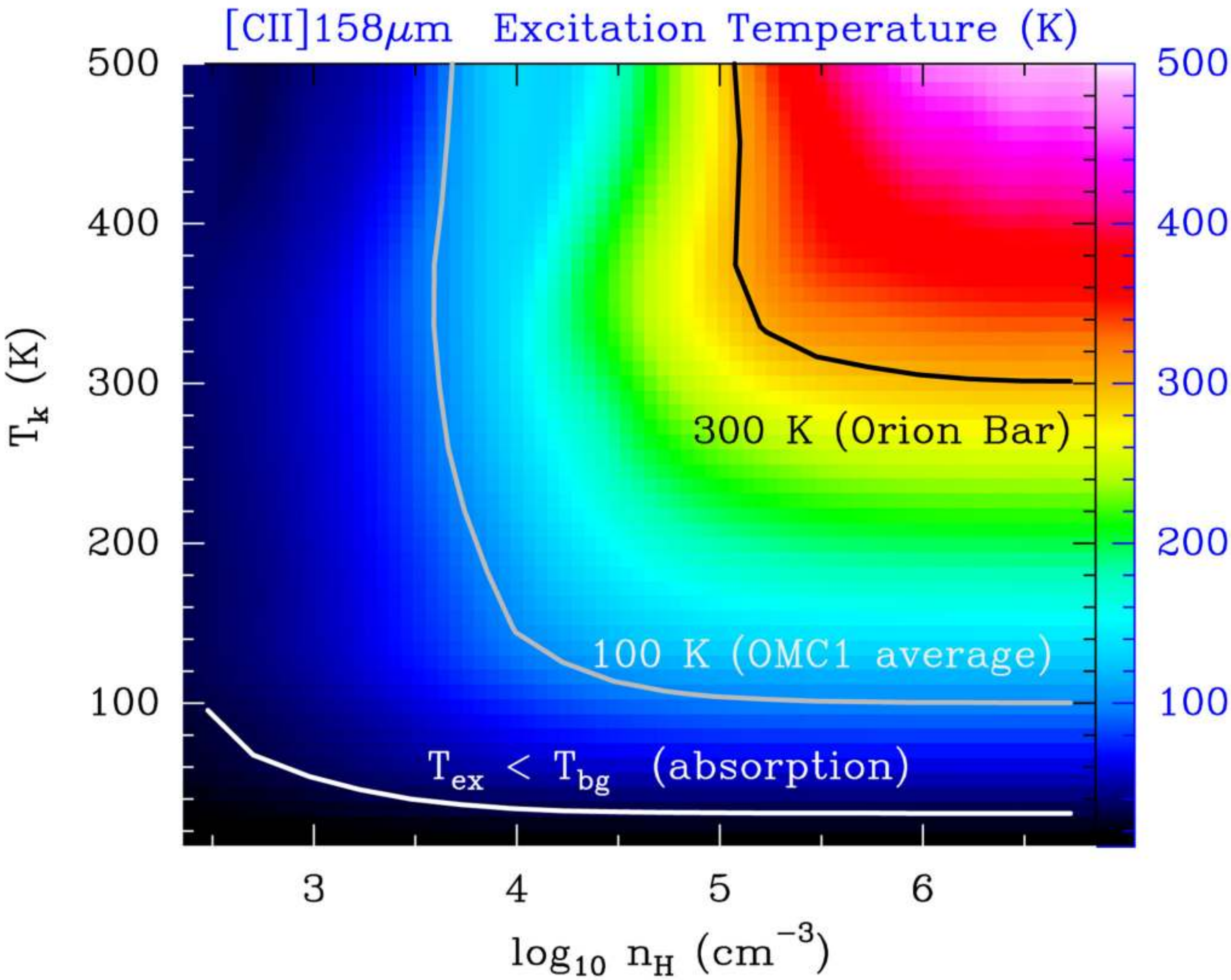

Figure 10.

Synthetic excitation temperatures for the [C II] 158 μm transition obtained from a grid of nonlocal non-LTE models (see text).

Europe PMC Funders Author Manuscripts

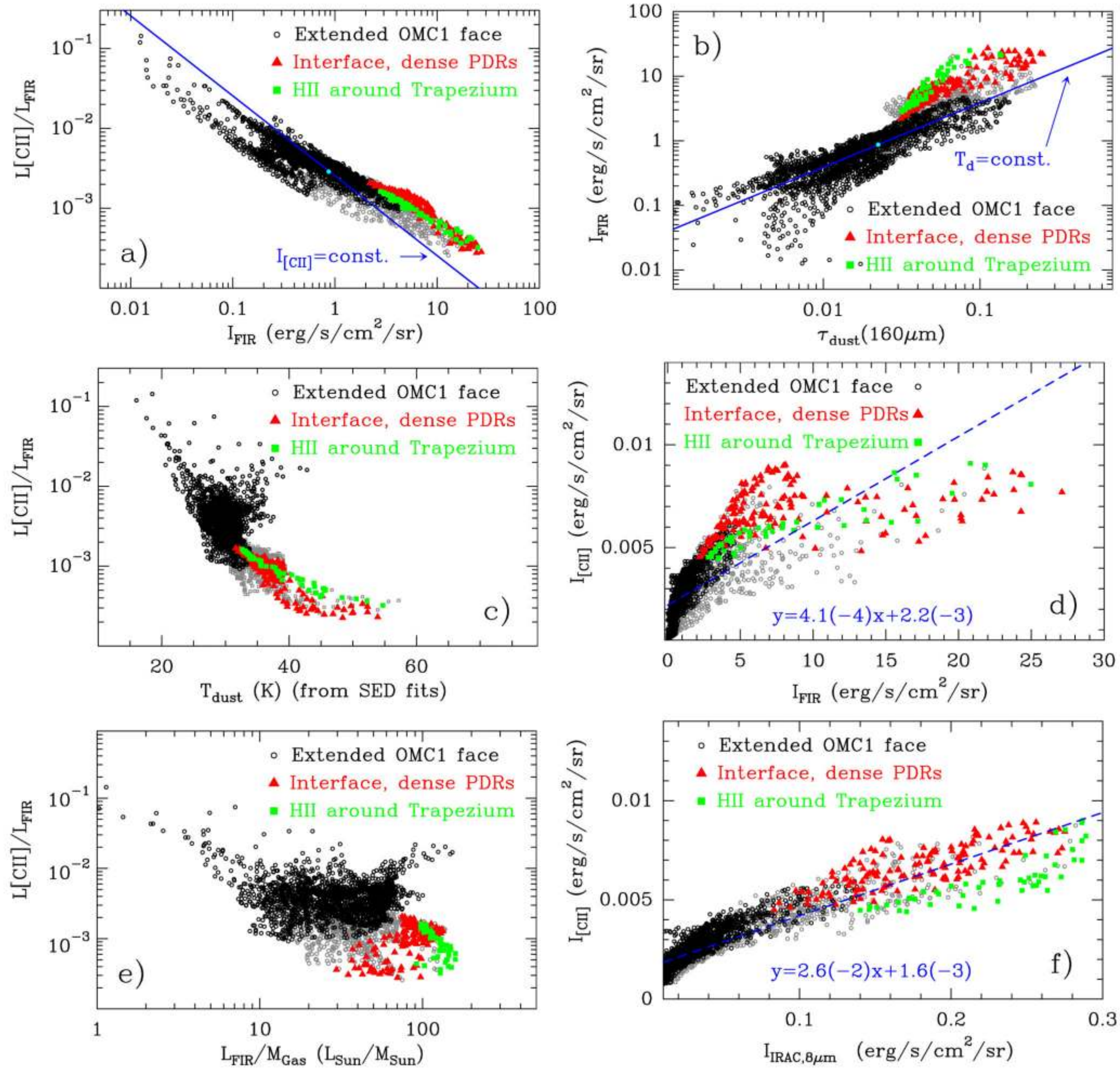

Figure 11.

Correlation plots extracted from the OMC 1 maps and convolved to a uniform 25″ resolution. Black points represent positions outside the 200″ (0.4 pc) radius circle ("extended cloud face" component). Green squares represent positions toward the H II region component around the Trapezium. Red triangles represent positions in the "dense PDR interface" annulus (see e.g., Figure 2). Gray points are other positions inside the 200″ (0.4 pc) radius circle that do not fall in the latter two categories. Two models (blue lines) are plotted in panels (a) and (b), one for a constant [C II] intensity cloud (a) and another for a cloud of constant T_d (b). Both models are defined to intercept the median $L[C\ II]/L_{FIR}$, I_{FIR} and $\tau_{d,160}$ of the map (cyan dots).

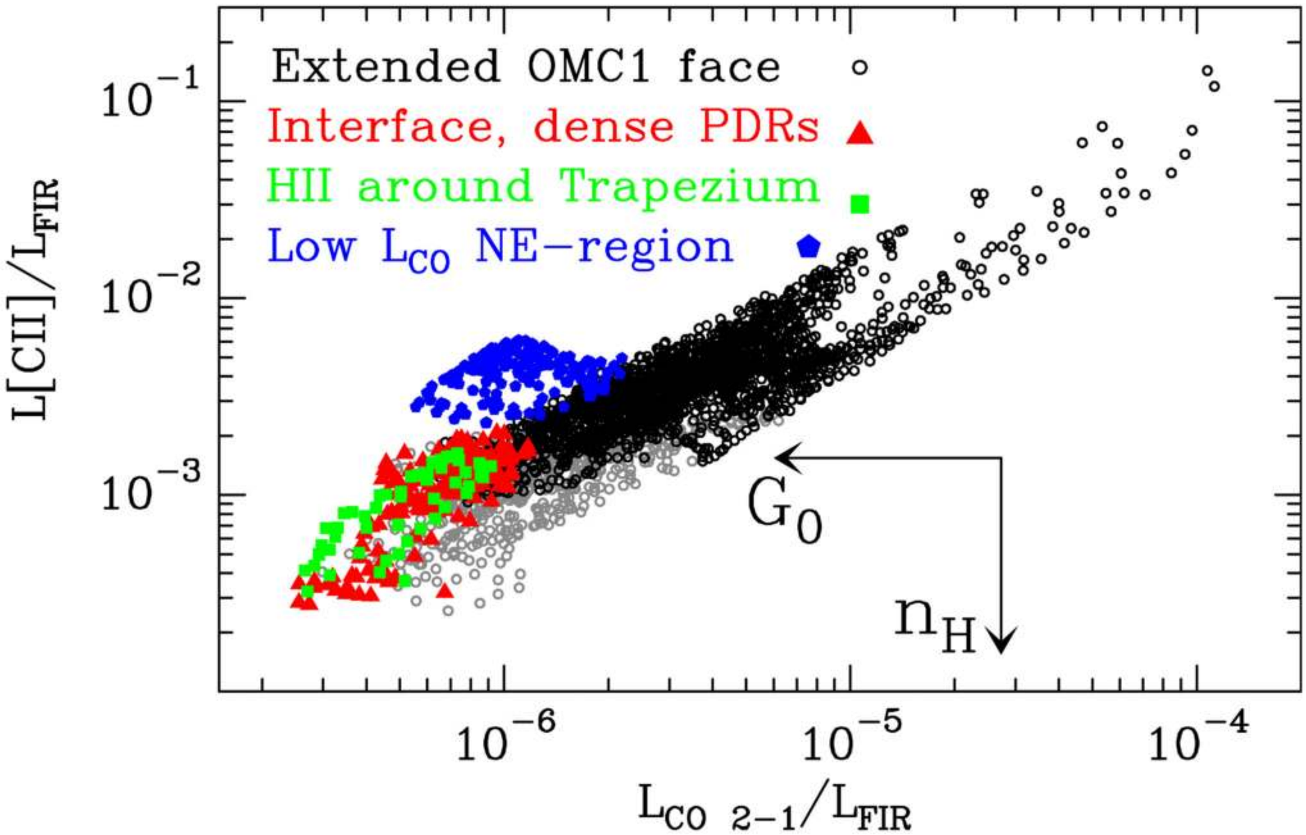

Figure 12.

Same as Fig. 11 but for L[C II]/L_{FIR} versus $L_{CO\ 2-1}/L_{FIR}$. The blue pentagons represent lines of sight of low L(CO) and high− L[C II]/L_{FIR} ratios (up to ~5000) at the northeast of the map, see Figures 8(c) and 8(e). Arrows show the approximate directions of increasing G_0 and increasing n_H expected from PDR models (e.g., Kaufman et al. 1999; Stacey et al. 2010).

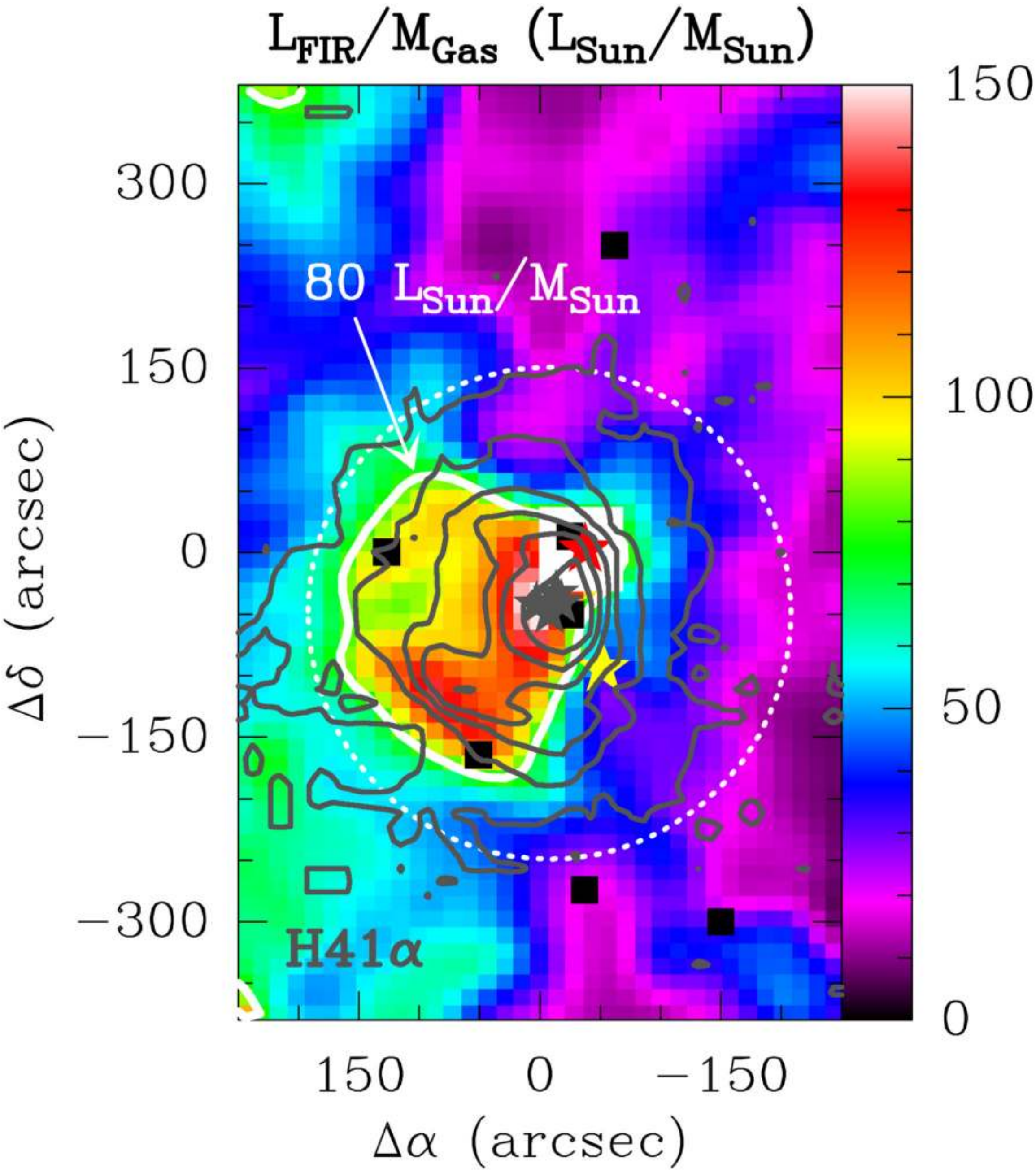

Figure 13.

Spatial distribution of the L_{FIR}/M_{Gas} ratio in units of $L_{\odot} M_{\odot}^{-1}$ per pixel (colored map) and H41α integrated intensity map in gray contours (from 2 to 22 K km s^{-1} in steps of 4 K km s^{-1}). The white thick curve shows the L_{FIR}/M_{Gas}=80$L_{\odot} M_{\odot}^{-1}$ iso-contour. Note the good correspondence between the ionized gas emission and the regions of high L_{FIR}/M_{Gas} ratios. The red, yellow and the gray stars show the position of the Orion hot core, Orion S and the Trapezium stars respectively. The black squares show the positions of the spectra shown in Figure 3.

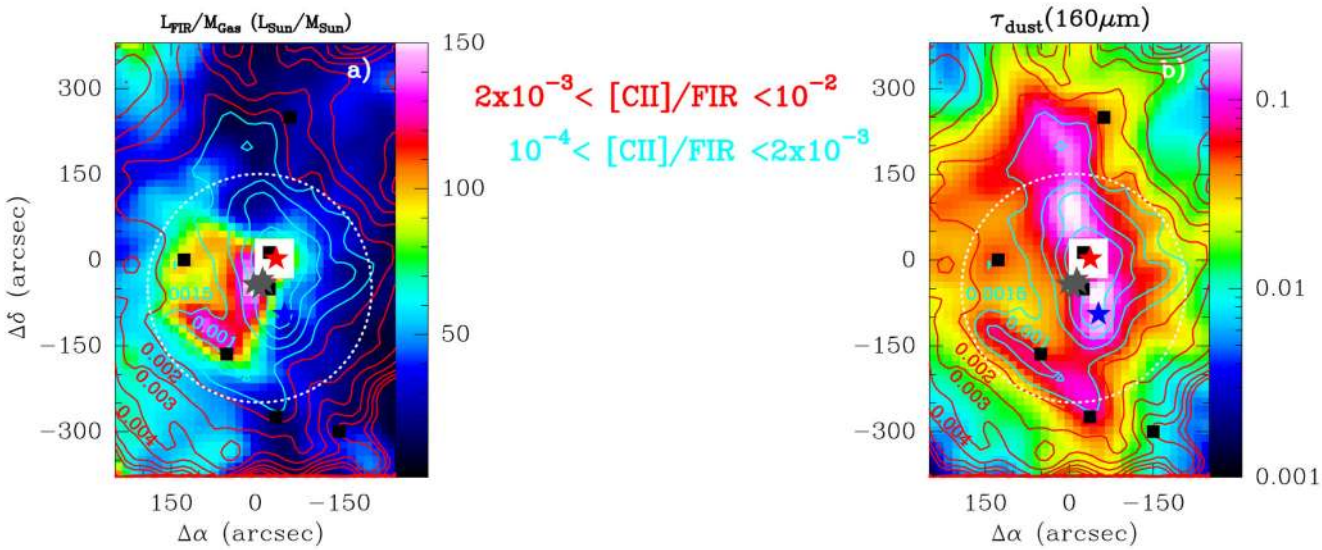

Figure 14.

Spatial distribution of two regimes found for the L[C II]/L_{FIR} luminosity ratio. Cyan contours for low L[C II]/L_{FIR} ratios, 10^{-4}–$1.5 \cdot 10^{-3}$ toward the core of OMC 1, and red contours for high ratios, 2×10^{-3}–10^{-2} toward the extended cloud component (the L[C II]/L_{FIR} ratio increases from the center of the map and outwards). (*a*) The colored map shows the L_{FIR}/M_{Gas} ratio, which to a first-approximation traces ionized gas and the ionization parameter U. (*b*) The colored map shows the spatial distribution of the dust opacity at 160 μm. The red, blue and the gray stars show the position of the Orion hot core, Orion S and the Trapezium stars respectively. The black squares denote the positions of the spectra shown in Figure 3.

Europe PMC Funders Author Manuscripts

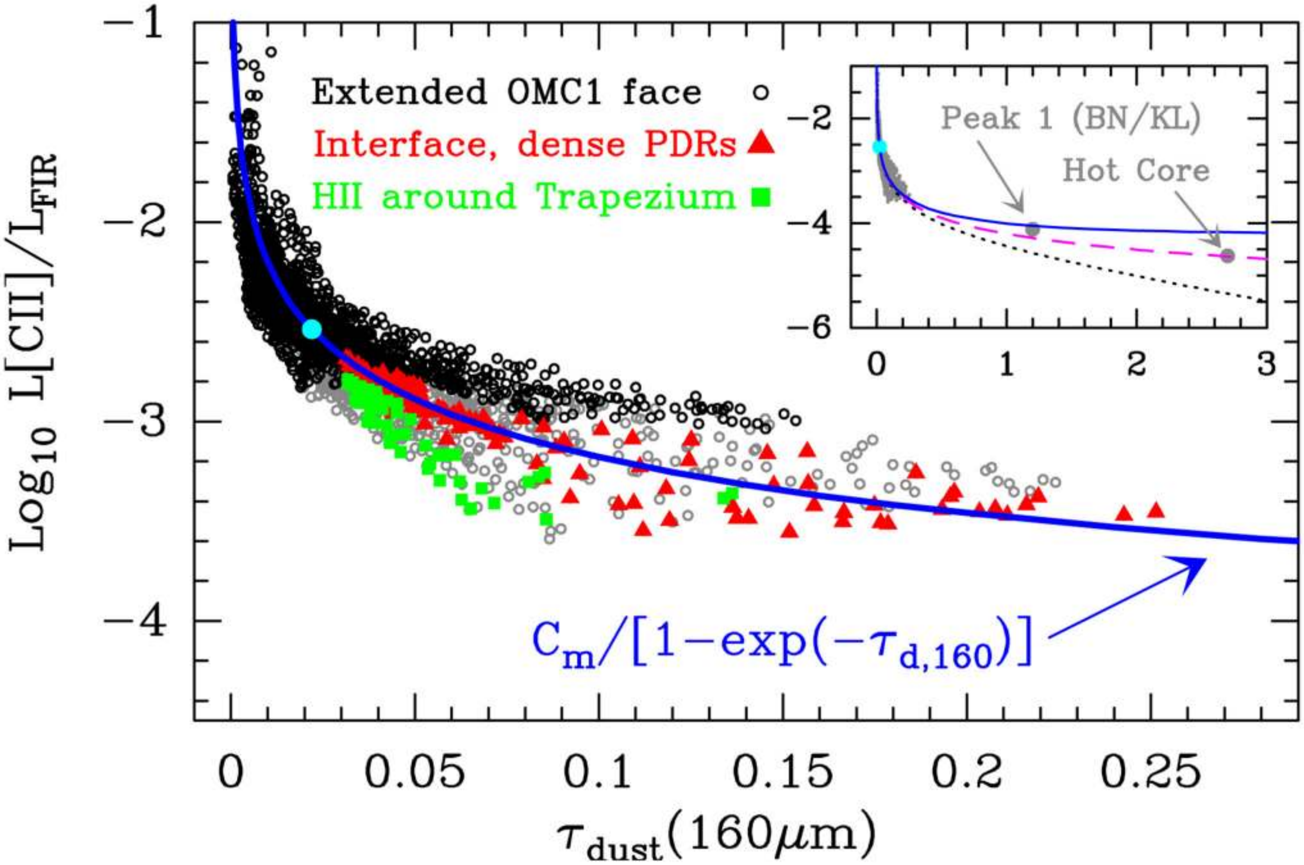

Figure 15.

Observed L[C II]/$L_{\rm FIR}$ ratios as a function of the 160 μm dust opacity. The different template regions are defined in Section 3.2. The inset panel shows an extension to higher dust opacity positions toward BN/KL. The blue continuos, magenta dashed, and black dotted curves show models of constant I[C II]/$B(T_{\rm d})$ emission for different assumptions of the [C II] emission location with respect to the cloud dust emission: [C II] in the foreground surface (as in OMC 1), mixed C^+ gas and grains, and embedded [C II] sources behind the cloud respectively (see sketch in Figure 16). Models are defined to intercept the median L[C II]/$L_{\rm FIR}$ and $\tau_{\rm d,160}$ values of the map (cyan dot).

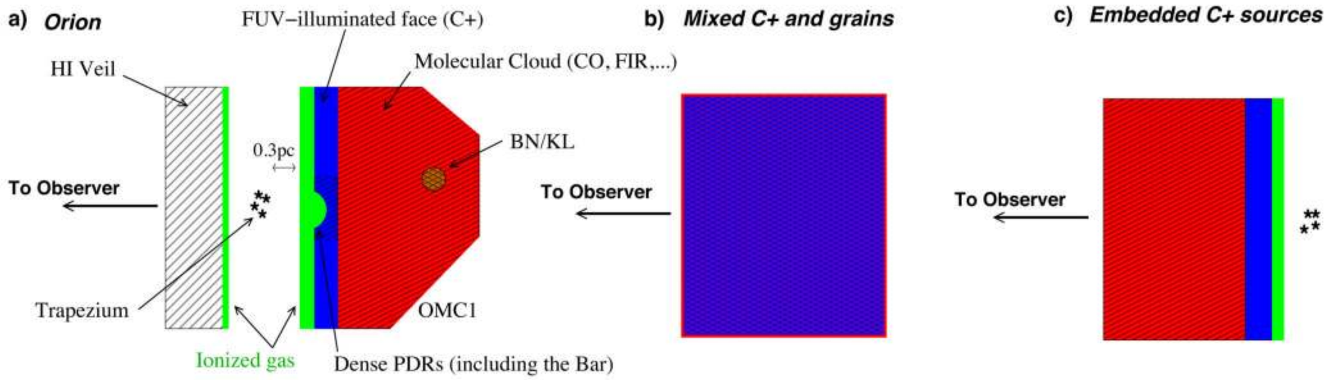

Figure 16.

(*a*) Simplified geometry (not to scale) of OMC 1 (red, molecular gas and dust), the FUV-illuminated cloud face (blue, dominating the [C II] emission), dense ionized gas in the H II region surrounding the Trapezium (green), and the atomic Veil (shaded, producing foreground H I absorption). The observed [C II] emission, $I_{[CII]}$, reaches the observer (to the left) almost unattenuated. At a given position, the observed ~160 μm dust emission is $B_{160}(T_d)(1 - e^{-\tau_{d,160}})$, where $\tau_{d,160}$ is the ~160 μm dust opacity along the entire line of sight. (*b*) *Mixed* C^+ and dust grains along the line of sight. In this case $I_{[CII]}=I_{0,[CII]}(1 - e^{-\tau_{d,160}})/\tau_{d,160}$, where $I_{0,[CII]}$ is the unattenuated [C II] emission. (*c*) [C II] sources *embedded* behind large columns of dust. In this case $I_{[CII]}=I_{0,[CII]}\, e^{-\tau_{d,160}}$.

Europe PMC Funders Author Manuscripts

Table 1

Spectroscopic parameters of the lines discussed in this work

Species	Transition	Frequency (GHz)	E_u/k (K)	A_{ij} (s^{-1})
$^{12}C^{+}$	$^2P_{3/2}$-$^2P_{1/2}$	1900.5369[a]	91.21	2.32(−6)
$^{13}C^{+}$	$^2P_{3/2}$-$^2P_{1/2}$			
	F=1-0	1900.9500[a,b]	91.23	1.55(−6)
	F=2-1	1900.4661[a,b]	91.25	2.32(−6)
	F=1-1	1900.1360[a,b]	91.23	7.73(−7)
CO	J=2-1	230.5379	16.60	6.92(−7)
H41α	n=42-41	92.0344[c]	89.50	4.85(+1)

[a]**Note.** — From Cooksy et al. (1986).

[b]See Ossenkopf et al. (2013) for corrected relative line-strengths.

[c]From Lilley & Palmer (1968).

Europe PMC Funders Author Manuscripts

Table 2

Average physical parameters toward different regions of OMC 1

	$L_{[C\,II]}/L_{FIR}$	$L_{CO\,2-1}/L_{FIR}$	$L_{[C\,II]}/L_{CO\,2-1}$	L_{FIR}/M_{Gas} ($L_{\odot}$=$M_{\odot}$)	G_0 [b] (Habing field)	$\tau_{d,160}$
OMC1 (full map[a])	3.8(5.4)×10^{-3}	3.6(6.2)×10^{-6}	1200(900)	43(27)	7.5×10^{3}	0.03(0.03)
Extended Cloud (R>0.4 pc)	4.7(6.0)×10^{-3}	4.5(7.5)×10^{-6}	1400(900)	35(20)	3.2×10^{3}	0.02(0.02)
Dense PDR interface (0.16<R<0.24 pc annulus[a])	1.1(0.5)×10^{-3}	6.6(2.2)×10^{-7}	1600(500)	87(24)	3.3×10^{4}	0.08(0.05)
Toward H II around Trapezium (R<0.1 pc)	9.3(3.9)×10^{-4}	5.4(1.8)×10^{-7}	1700(400)	126(18)	3.3×10^{4}	0.05(0.02)

Note. — Average values over the different *template* cloud regions defined in Section 3.2. Numbers in parenthesis represent the standard deviation (1σ) of each sample. L_{FIR} refers to the 40-500 μm range.

[a]The central Orion BN/KL region (50′×50′) is not included in the computation of the average values due to saturation of the photometric measurements. A low L[C ii]/L_{FIR}≃(2-8)×10^{-5} luminosity ratio and $t_{d,160}$≃1-3 was inferred from *Herschel*/PACS spectroscopic observations (Goicoechea et al. 2015). The mean L[C II]/$L_{CO\,2-1}$ ratio in this region is ~270.

[b]Estimated from I_{FIR} and Equation 3.